

THE TIME VARIABILITY OF GEOMETRICALLY THIN BLACK HOLE ACCRETION DISKS. I. THE SEARCH FOR MODES IN SIMULATED DISKS

CHRISTOPHER S. REYNOLDS AND M. COLEMAN MILLER

Department of Astronomy and the Maryland Astronomy Center for Theory and Computation, University of Maryland, College Park, MD 20742-2421, USA
Received 2007 August 13; accepted 2008 October 20; published 2009 February 20

ABSTRACT

We present a detailed temporal analysis of a set of hydrodynamic and magnetohydrodynamic (MHD) simulations of geometrically thin ($h/r \sim 0.05$) black hole accretion disks. The black hole potential is approximated by the Paczynski–Wiita pseudo-Newtonian potential. In particular, we use our simulations to critically assess two widely discussed models for high-frequency quasi-periodic oscillations (QPOs), global oscillation modes (diskoseismology), and parametric resonance instabilities. We find that initially disturbed hydrodynamic disks clearly display the trapped global g -mode oscillation predicted by linear perturbation theory. In contrast, the sustained turbulence produced in the simulated MHD disks by the magnetorotational instability does not excite these trapped g -modes. We cannot say at present whether the MHD turbulence actively damps the hydrodynamic g -mode. Our simulated MHD disks also fail to display any indications of a parametric resonance instability between the vertical and radial epicyclic frequencies. However, we do see characteristic frequencies at any given radius in the disk corresponding to local acoustic waves. We also conduct a blind search for *any* QPO in a proxy light curve based on the instantaneous mass accretion rate of the black hole, and place an upper limit of 2% on the total power in any such feature. We highlight the importance of correcting for secular changes in the simulated accretion disk when performing temporal analyses.

Key words: accretion, accretion disks – black hole physics – magnetic fields – X-rays: binaries

Online-only material: color figures

1. INTRODUCTION

Rapid X-ray variability is a ubiquitous characteristic of accretion onto black holes. Aperiodic X-ray fluctuations are seen from both galactic black hole binaries (GBHBs) and active galactic nuclei (AGNs) and, accounting for the inverse scaling of all relevant frequencies with black hole mass, appear to have similar characteristics (Uttley et al. 2005; McHardy et al. 2006). While it is highly tempting to relate this variability to the magnetohydrodynamic (MHD) turbulence that is believed to drive the accretion process (Balbus & Hawley 1991, 1998), the exact physical processes underlying the observed fluctuations remain mysterious.

GBHBs also display quasi-periodic oscillations (QPOs) in their X-ray light curves (see review by McClintock & Remillard 2003).¹ The high-frequency QPOs (HFQPOs) that are seen in the very high (or steep power law; McClintock & Remillard 2003) state of GBHBs are of particular interest. The HFQPOs have quality factors of few to 10, centroid frequencies of order of 100Hz, and appear to be imprinted on the hard X-ray tail of the spectrum rather than the thermal disk emission. The fact that their frequencies are stable and at least loosely comparable with the orbital frequency at the innermost stable circular orbit (ISCO) around the black hole suggests that their properties are set by the relativistic portions of the gravitational potential. This gives them enormous promise as a diagnosis of black hole mass and spin.

However, the utility of HFQPOs to relativistic astrophysics is severely limited by the lack of a compelling theoretical framework in which to interpret measurements of the frequencies, quality factors, and rms powers. There exist well defined

geodesic frequencies (i.e., the orbital, radial epicyclic, and vertical epicyclic frequencies) at any given radius in the accretion disk. However, these frequencies (as well as all nontrivial linear combinations) change with the radius, and it is not clear why the frequencies of any one particular radius would be preferentially displayed in the overall power spectrum.

HFQPOs are commonly found in pairs with an approximate 3:2 frequency ratio, and this has been used to suggest that a particular radius is picked out due to a resonance. In the parametric resonance model (Abramowicz & Kluźniak 2001, 2003; Abramowicz et al. 2002, 2003), there is a resonance in the disk at the radius where the radial epicyclic frequency and vertical epicyclic frequency are in small integer ratios. As discussed below, the strongest resonance occurs when these frequencies are in a 3:2 ratio, at least in the simplest manifestation of this model. Other resonance models have been examined by Rezzolla et al. (2003a, 2003b) and Kato (2004a, 2004b, 2004c).

Another interesting possibility is that the HFQPOs are global oscillation modes of the accretion disk (i.e., “diskoseismic” modes). Global modes have been examined analytically (using linear theory) on a hydrodynamic background in spacetimes that are pseudo-Newtonian (Okazaki et al. 1987; Nowak & Wagoner 1991, 1992, 1993; Marković & Lamb 1998), Schwarzschild (Kato & Fukue 1980), and Kerr (Kato 1990, 1991, 1993; Kato & Honma 1991; Perez et al. 1997; Silbergleit et al. 2001; Wagoner et al. 2001; Ortega-Rodriguez et al. 2001). Three classes of modes are recovered corresponding to pressure modes (p -modes), inertial modes (conventionally referred to as g -modes even though the restoring force results from rotation or inertia, depending on the frame of reference; J. Pringle 2008, private communication), and warping/corrugation modes (c -modes). For plausible masses and spins, the fundamental ($m = 0$) g -mode was quickly identified as a good candidate for the first

¹ Very recently, the first convincing case of a QPO in an AGN was reported by Gierlinski et al. (2008).

HFQPO discovered, the 67 Hz oscillation found in the system GRS 1915 + 105 (Nowak et al. 1997). Current diskoseismology theory does not provide a natural explanation of HFQPO pairs with small-integer ratios; however, all present analyses are conducted using linear theory whereas these HFQPO pairs would likely arise from mode coupling that would only be revealed by a nonlinear analysis.

Clearly, many open questions concerning the physics of X-ray variability remain, including the correct interpretation of HFQPOs. The current dominant paradigm for understanding black hole accretion is that the magnetorotational instability (MRI; Balbus & Hawley 1991) drives powerful MHD turbulence, and correlated Maxwell stresses within this turbulence mediate the outward transport of angular momentum that allows accretion to proceed. However, the connection between the MHD turbulence paradigm and models for the aperiodic and quasi-periodic variabilities remains highly uncertain. For example, can the MHD turbulence naturally produce the rms–flux relation noted in most black hole X-ray light curves (Uttley & McHardy 2001) and/or the log-normal flux distribution found in Cygnus X-1 (Uttley et al. 2005)? Are diskoseismic modes excited by turbulent fluctuation (Nowak & Wagoner 1993), or does the turbulence act to damp such modes (Arras et al. 2006)? Do the Maxwell stresses couple radial and vertical motions in such a way as to excite parametric resonance instabilities of the type identified by Abramowicz & Kluźniak (2001) or any other resonant phenomena? Does the fact that the HFQPOs are imprinted on the high-energy tail provide a fundamental clue to their origin, or is it a generic consequence of any oscillating thermal accretion disk surrounded by a Comptonizing corona (Lehr et al. 2000)?

In this paper, we use a set of global hydrodynamic and MHD simulations of geometrically thin accretion disks in a pseudo-Newtonian potential to begin an exploration of these issues. Our canonical MHD simulation represents a thinner disk, and is run for more orbits, than any previously published well resolved three-dimensional MHD disk simulation. This allows us to conduct a more extensive study of the temporal variability of such disks than has previously been attempted. In Section 2, we give a brief review of the theory of both local and global hydrodynamic modes of black hole accretion disks, as well as the parametric resonance instability model for HFQPOs. Section 3 presents our study of ideal (inviscid) hydrodynamic disks, both with imposed axisymmetry and in full three dimensions. We find prominent trapped g -modes in the axisymmetric simulations that remain (albeit with diminished amplitude) in the full three-dimensional case. We then study the MHD case in Section 4, where we find that the turbulence excites neither the diskoseismic modes nor the parametric resonances discussed above. Instead, we find that the turbulence excites local hydrodynamic waves of the type elucidated by Lubow & Pringle (1993; hereafter LP93). We discuss our results, including a comparison with previous work, in Section 5 and conclude in Section 6.

2. THEORETICAL PRELIMINARIES

Here we provide a brief review of some previously established theoretical results that are pertinent to this paper.

2.1. Local Oscillations and Waves in Accretion Disks

There is a very extensive literature on oscillations and waves in accretion disks. Here, we focus on just those aspects of the

field that turn out to be relevant for the interpretation of our simulation, which have been elucidated most clearly by LP93.

LP93 studied three-dimensional wave propagation in accretion disks ignoring self-gravity. In the case where one ignores vertical motions, they show that radial waves obey the well known dispersion relation:

$$\omega^2 = \kappa^2 + c_s^2 k^2, \quad (1)$$

where c_s is the sound speed (assumed, in this case, to be purely a function of r) and κ is the radial epicyclic frequency given by $\kappa^2 = 4\Omega^2 + r \partial\Omega^2/\partial r$ (also see Binney & Tremaine 1987). Here, $\Omega(r)$ is the angular frequency of the background Keplerian flow. LP93 proceeded to study the propagation of axisymmetric waves in the case where the atmosphere has a locally isothermal vertical structure. They find two types of waves. There are low-frequency gravity waves for which

$$0 < \omega < \Omega. \quad (2)$$

There are also high-frequency acoustic waves that have

$$\omega^2 > (n\gamma + 1)\Omega^2, \quad (3)$$

where $n = 0, 1, 2, \dots$ and γ is the adiabatic index. In the special case of purely vertical perturbations, the inequality becomes an equality:

$$\omega^2 = (n\gamma + 1)\Omega^2. \quad (4)$$

The $n = 0$ mode corresponds to a bulk vertical displacement of the disk and subsequent vertical oscillation at the vertical epicyclic frequency, which, in the analysis of LP93 and in all analyses performed in this paper, coincides with the orbital frequency. In general, the n th mode has n vertical nodes (i.e., locations where the vertical velocity perturbation vanishes), and is either even or odd depending on whether n is even or odd, respectively.

As discussed in Section 4, our simulations demonstrate the effectiveness with which MHD turbulence excites these local acoustic waves.

2.2. Global Oscillation Modes of an Accretion Disk

As discussed in Section 1, several groups have studied the global oscillation of black hole accretion disks using linear perturbation theory, identifying three classes of the normal mode (g -modes, p -modes and c -modes). Trapped g -modes have received particular attention as a possible source of the HFQPO, although the other families of modes may well be relevant. Here we review some of the basic results of these analyses, following the approach of Nowak & Wagoner (1991, 1992; hereafter NW91 and NW92, respectively). The NW91 and NW92 analyses are not fully relativistic; instead, they employ a pseudo-Newtonian potential. Thus, these analyses can be readily compared with our pseudo-Newtonian simulations. We also note that full general relativistic MHD simulations have typically yielded results for slowly rotating black holes that are very similar to those obtained with pseudo-Newtonian potentials (e.g., Gammie et al. 2003; De Villiers & Hawley 2003).

NW91 and NW92 used a Lagrangian formalism (Friedman & Schutz 1978) and a WKB approximation to derive the linearized equations describing perturbations of an inviscid hydrodynamic thin accretion disk about a pure Keplerian background state. They also initially examined the special case of purely radial oscillations and found the standard dispersion

relation of disk theory (Equation (1)). Given that the gravity-modified p -modes described by this dispersion relation become evanescent when $\omega^2 < \kappa^2$, global p -modes can be trapped between the ISCO (where $\kappa = 0$) and the radius at which $\omega = \kappa$. In practice, however, the “leaky” nature of the ISCO would seem to make the trapping of these modes ineffective.

The more general case, including perturbations that have vertical as well as radial motions, yields more promising results. NW92 examined the linearized equations describing the behavior of the scalar potential

$$\delta u \equiv \delta P / \rho, \quad (5)$$

where δP is the Eulerian variation in the pressure. They showed that the linearized equations are approximately separable into radial and vertical equations, with the separation constant being a slowly varying function of r , $\Upsilon(r)$. The general dispersion relation for these modes becomes

$$[\omega^2 - \gamma \Upsilon(r) \Omega^2](\omega^2 - \kappa^2) = \omega^2 c_s^2 k^2. \quad (6)$$

Assuming that $\gamma \Upsilon \Omega^2 > \kappa^2$, nonevanescant solutions exist for $\omega^2 > \gamma \Upsilon \Omega^2$ (predominantly radial p -modes) or $\omega^2 < \kappa^2$ (predominantly vertical g -modes). Through this analysis, NW92 identified a class of global g -modes that are trapped between two evanescent regions, $r < r_-$ and $r > r_+$, where $\kappa(r_{\pm}) = \omega$. In other words, these modes are trapped under the peak of the epicyclic frequency. They principally focused on the $m = 0$ (axisymmetric) modes, and showed that the mode frequency is only *slightly* smaller than the maximum radial epicyclic frequency κ_{\max} . Radial harmonics of these modes are very closely spaced. Thus, the inner radius at which the mode becomes evanescent is still a finite distance (and, in plausible settings, several vertical scale heights) from the ISCO. This raises the interesting possibility of having appreciable power in such modes without significant leakage across the ISCO.

A major issue, however, is the effect of the turbulent MHD background state on these modes. The diskoseismic mode frequencies are comparable with the frequencies characterizing the expected MHD turbulent fluctuations (which is very different to the situation in the Sun, for example, where the observed helioseismic modes have frequencies that are four orders of magnitude higher than the turbulent turnover frequency). Thus, an MHD turbulent disk is likely to be a hostile environment for any diskoseismic modes. Furthermore, magnetic forces can lead to a rather gradual transition in flow properties around the ISCO, potentially worsening the leakage of the trapped g -modes. Considering these mode destruction/suppression mechanisms, it is reasonable to suppose that mode survival becomes easier in thinner disks since (1) the ratio of the typical turbulent cell size to the radial extent of the resonant cavity will decrease with disk thickness and (2) there are suggestions that the transition in flow properties around the ISCO is sharper in thinner disks (Reynolds & Fabian 2008; Shafee et al. 2008), thereby producing less mode leakage. This raises the possibility that a g -mode can be sustained against (or even fed by; Nowak & Wagoner 1993) the turbulence in a sufficiently thin disk.

Previously published global MHD disk simulations (e.g., Hawley & Krolik 2001) have modeled flows as thin as $h/r \sim 0.1$ and have not reported diskoseismic modes. However, these authors did not conduct a directed search for such modes and hence it is not possible to say that the modes were really not present. Careful examination of local “shearing-box” simulations have indeed failed to find trapped g -modes

associated with MHD turbulence (Arras et al. 2006), but this issue has yet to be examined in a global thin-disk setting. Searching for and characterizing these trapped g -modes in global thin-disk simulations will be a major theme of our paper.

2.3. Parametric Resonance

From the point of view of explaining HFQPOs, the need for global oscillation modes is diminished if some process does indeed select special radii in the accretion disk. As discussed in Section 1, the discovery of pairs of HFQPOs with small integer ratios has prompted several groups to examine resonance models. In particular, we shall briefly review the parametric resonance model of Abramowicz & Kluźniak (Abramowicz & Kluźniak 2001, 2003; Abramowicz et al. 2002, 2003).

We begin by considering an accretion disk in which the flow deviates only slightly from the Keplerian so that the position of a fluid element (in spherical polar coordinates) is given by

$$r(t) = r_0 + \delta r(t), \quad \theta(t) = \frac{1}{2}\pi + \delta\theta(t), \quad \phi(t) = \Omega t. \quad (7)$$

We have specialized to the case of axisymmetric perturbations. By expanding the resulting equations of motion to third order (and wrapping up the nongravitational forces into two unspecified force functions), one finds a Mathieu-type equation of motion:

$$\delta\theta_{,tt} + \Omega^2[1 + a \cos(\kappa t)]\delta\theta + \lambda \delta\theta_{,t} = 0, \quad (8)$$

where a is a small constant that describes the coupling between the vertical and radial perturbations and λ is a (small) damping constant. Here, we have specialized the equations of Abramowicz et al. (2003; hereafter A2003) to the case where the vertical epicyclic frequency is the same as the orbital frequency. This is valid for a nonspinning black hole and, in particular, the pseudo-Newtonian potential that we use for the simulations in this paper.

One expects a system described by Equation (8) to exhibit a parametric resonance instability when $\kappa = 2\Omega/n$, where n is a nonzero positive integer. Given that black hole potentials always have $\kappa < \Omega$, the smallest value of n for which the resonance condition is obeyed is $n = 3$, that is, $\kappa = 2\Omega/3$. This is expected to be the strongest of the set of resonances. It is interesting that the fundamental “test-particle” frequencies at this resonant radius have a 3:2 frequency ratio in agreement with observations of HFQPO pairs. For the Paczynski–Wiita (PW) pseudo-Newtonian potential we use in our simulations (Paczynski & Wiita 1980; hereafter PW),

$$\Phi = -\frac{GM}{r - 2r_g}, \quad r_g \equiv \frac{GM}{c^2}, \quad (9)$$

we have

$$\Omega = \frac{1}{r - 2r_g} \sqrt{\frac{GM}{r}} \quad (10)$$

and

$$\kappa = \sqrt{\frac{GM(r - 6r_g)}{r(r - 2r_g)^3}}. \quad (11)$$

Hence, the 3:2 resonance occurs at $r = 9.2r_g$. It must be noted, however, that a full integration of a toy problem by A2003 reveals that higher order effects shift the location of

Table 1
Summary of the Hydrodynamic (HD) and MHD Simulations Discussed in This Paper

Run (1)	dim (2)	h_2/r_{isco} (3)	r -domain (r_g) (4)	z -domain (r_g) (5)	ϕ -domain (6)	$n_r \times n_z (\times n_\phi)$ (7)	T_{stop} (r_g/c) (8)
HD2d_1	2	0.05*	(4,16)	(-1.5,1.5)	–	256×128	12320
HD2d_1hr	2	0.05*	(4,28)	(-1.5,1.5)	–	1024×256	12320
HD2d_2	2	0.025*	(4,16)	(-0.75,0.75)	–	512×128	12320
HD2d_3	2	0.1*	(4,16)	(-3,3)	–	256×128	12320
HD3d_1	3	0.05*	(4,16)	(-1.5,1.5)	(0, $\pi/6$)	$240 \times 128 \times 32$	12320
MHD_1	3	0.05	(4,16)	(-3,3)	(0, $\phi/6$)	$240 \times 256 \times 32$	38800
MHD_2	3	0.05	(4,16)	(-1.5,1.5)	(0, $\phi/6$)	$240 \times 128 \times 32$	38800
MHD_2hr	3	0.05	(4,16)	(-1.5,1.5)	(0, $\phi/3$)	$480 \times 256 \times 64$	5236
MHD_3	3	0.05	(4,28)	(-1.5,1.5)	(0, $\phi/6$)	$960 \times 128 \times 32$	11400

Notes. Column (1) gives the designation of the simulation. Column (2) lists the dimensionality of the simulation. Column (3) gives the fractional disk thickness at the ISCO; the asterisk (*) denotes that the simulation was started with an initial vertical structure that is slightly out of equilibrium in order to seed subsequent oscillation modes (as described in the text). Columns (4)–(6) list the r -, z - and ϕ - domains of the simulation box, respectively. Column (7) gives the number of computational zones within the domain. Column (8) lists the run time of the simulated disk.

the resonance, making the ratio of the epicyclic frequencies extremely sensitive to the strength of the coupling between the r and θ perturbations. While A2003 suggested that this sensitivity is a strength of the model, allowing application to HFQPO pairs in neutron star systems that do not have simple integer ratios, it inevitably diminishes the power of this model to explain black hole systems. In addition, there is currently no physical model of the coupling between the radial and vertical motions. The simulations described in this paper allow us to assess whether magnetic forces couple these motions in such a way as to drive a parametric resonance instability.

3. HYDRODYNAMIC DISKS

3.1. Initial Comments

In the remainder of this paper, we construct and analyze numerical simulations of thin disks in order to examine their variability properties, focusing on the presence of local and global modes, as well as parametric resonances. Of course, real accretion disks are believed to require at least an MHD-level description in order to capture the MRI-driven turbulence that transports angular momentum and drives accretion. MHD simulations are addressed in Section 4. However, it is useful to begin with a discussion of ideal hydrodynamic models in order to help isolate the various physical effects present in these complex systems. This will be the focus of this section.

In order to allow us to perform a set of simulations with modest-to-high resolution, we begin with two-dimensional (axisymmetric) hydrodynamic simulations. We expect (and indeed show) that these axisymmetric models are well suited for studying the fundamental $m = 0$ g -mode. However, once we move to MHD, Cowling’s antidynamo theorem (Cowling 1957) leads to qualitatively different behavior in axisymmetric compared with full three-dimensional simulations. Hence, all of the MHD models that we shall describe are performed in three dimensions. Since we will be directly comparing results (e.g., g -mode amplitudes) between the hydrodynamic and MHD simulations, we also need to perform a “bridging” three-dimensional hydrodynamic simulation.

3.2. Basic Simulation Setup

To make the problem tractable despite the severe resolution requirements imposed by the geometrical thinness of the accre-

tion disk, we choose to focus on only the most essential aspects of the physics. From the discussion in Section 2, it is clear that the essential aspect of the relativistic potential that must be captured is the nature of the radial epicyclic frequency (e.g., that it goes to zero at some finite radius and hence produces an ISCO at that radius). In this sense, the PW potential (Equation (9)) is a good approximation for the gravitational field of a nonrotating black hole; its ISCO (at $6r_g$) and marginally bound orbit (at $4r_g$) are both at the same radius as in the Schwarzschild geometry. We also simplify the simulations by neglecting all radiation processes (radiative heating, radiative cooling, radiative transfer, and the dynamical effects of radiation pressure). In place of a full energy equation, the gas is given an adiabatic equation of state with $\gamma = 5/3$.

All simulations are performed in cylindrical polar coordinates (r, z, ϕ). The initial condition consists of a disk with a constant midplane density ($\rho_0 = 1$) for $r > r_{\text{isco}}$. The initial density scale height of the disk is assumed to be constant with the radius, implying a sound speed that falls off with radius as approximately $r^{-3/2}$. There are two motivations for choosing to model a “constant-h” disk: (1) such a choice is well suited to the cylindrical symmetry of our coordinate grid and (2) according to the standard model of Shakura & Sunyaev (1973), the radiation-pressure-dominated disks of real accreting black holes are likely to maintain an approximately constant scale height in their innermost regions. In more detail, the vertical structure of the disk is given by

$$\rho(r, z) = \rho_0 \exp\left(-\frac{z^2}{2h_1^2}\right), \quad (12)$$

$$p(r, z) = \frac{GMh_2^2}{(R - 2r_g)^2 R} \rho(r, z), \quad (13)$$

where r is the cylindrical radius, z is the vertical height above the disk midplane, and $R = \sqrt{r^2 + z^2}$. This corresponds to an isothermal atmosphere, which, when $h_1 = h_2$, is in vertical hydrostatic equilibrium in the PW potential. In order to give the disk an initial vertical kick, we set $h_1 = 1.2h_2$ (the values of h_2 for all of our runs are detailed in Table 1). Thus, the initial disk temperature is $\sim 20\%$ too cold for the density and pressure run, leading to a vertical collapse and bounce of the disk. The initial

density is set to zero for $r < r_{\text{isco}}$. The initial velocity field is everywhere set to

$$v_\phi = r\Omega = \frac{\sqrt{GM}r}{r - 2r_g}, \quad v_r = v_z = 0, \quad (14)$$

corresponding to rotation on cylinders and pure Keplerian motion for material on the midplane. We impose zero-gradient outflow boundary conditions on both the radial and the vertical boundaries of the simulation, that is, the fluid quantities in the ghost zones are set to the values of the neighboring active zone, and a “diode” condition is imposed on the component of the velocity perpendicular to the boundary that allows outflow but disallows inflow.

Table 1 details our hydrodynamic simulations. We perform four simulations in which strict axisymmetry is imposed at all times ($\partial/\partial\phi = 0$). These axisymmetric simulations were performed using the serial ZEUS-3D MHD code (Stone & Norman 1992a, 1992b) in its pure hydrodynamic axisymmetric mode. In our canonical axisymmetric run (HD2d_1), we set $h_2 = 0.3r_g$ (corresponding to $h_2/r = 0.05$ at the ISCO). To model the dynamics of the disk in a robust manner, our vertical domain must cover many scale heights; in our canonical run, the vertical domain is $z \in (-5h_2, +5h_2)$. We place 128 uniformly spaced grid cells in this vertical direction, giving 13 cells per scale height. This allows us to resolve hydrodynamic waves with wavelengths of $\sim 0.5h_2$ or greater. The vertical resolution requirements force us to consider a limited radial domain. In the canonical simulation, the radial domain extends from $4r_g$ (i.e., well within the plunge region) to $16r_g$ and should correspond to the range of radii where trapped diskoseismic modes or A2003-type resonances occur. Tolerating a grid-cell aspect ratio of ~ 2 , we place 256 uniformly spaced radial cells in this radial domain. The simulation was evolved for a time $200T_{\text{isco}}$, where

$$T_{\text{isco}} \approx 61.6 GM/c^3, \quad (15)$$

is the orbital period at the ISCO.

In order to test the robustness of the results discussed below to resolution and the limited radial domain, we performed a second simulation (HD2d_1hr) in which the spatial resolution was doubled (i.e., the size of each voxel was halved in both the radial and the vertical dimensions) and the radial domain extended out to $28r_g$. We also performed two additional axisymmetric simulations employing the same setup as the canonical simulation but with disks that are half (HD2d_2) and twice (HD2d_3) the thickness (including appropriate modifications to the vertical domain and resolution; see Table 1).

As discussed above, we perform a three-dimensional hydrodynamic simulation in order to aid the later interpretation of the three-dimensional MHD simulations. The setup of our three-dimensional run (HD3d_1) is identical to that for the canonical two-dimensional run except that the computational domain has a ϕ -dimension. To reduce computational expense while capturing the essential physics, we simulate only a $\Delta\phi = 30^\circ$ wedge of the disk using 32 uniformly spaced grid cells, imposing periodic boundary conditions on the ϕ -boundaries. This three-dimensional simulation was performed using an MPI-parallelized version of ZEUS kindly supplied to us by Eve Ostriker (and similar to the ZEUS-MP code of Vernaleo & Reynolds 2006).

3.3. Axisymmetric Hydrodynamic Models and the Recovery of Trapped g -modes

We now discuss the evolution of the axisymmetric hydrodynamic simulations, beginning with the canonical simulation. Starting from the initial condition, the disk undergoes dynamical timescale variability because of pressure gradients, which push matter inside of the ISCO. The strong transients close to the ISCO launch outward-radially directed waves into the disk, which break rapidly to become rolls. This behavior can be seen in Figure 1. These high amplitude transients are short-lived, however, lasting only $\sim 10T_{\text{isco}}$. At subsequent times, the disk settles into a stationary state apart from small amplitude (and decaying) internal oscillations and a very weak accretion stream driven by the numerical viscosity.

In order to study the decay of the hydrodynamic fluctuations in a more quantitative manner, we start by computing the quantity

$$K = \int_{\mathcal{D}} \rho v_z^2 dV. \quad (16)$$

This quantity is particularly well suited to diagnose vertical oscillations of the disk, and will vanish once the hydrodynamic configuration has established a stationary state. In order to diagnose the state of the body of the disk (i.e., side-stepping issues of the outer radial boundary or the plunge region), we choose to compute this integral over a restricted domain \mathcal{D} consisting of the annulus $r \in (7r_g, 14r_g)$. The time dependence of $K/\max(K)$ for the canonical axisymmetric simulation (HD2d_1) and its high-resolution counterpart (HD2d_1hr) are shown in Figure 2. The rapid initial decline of $K(t)$ is very similar for these two simulations and corresponds to the strong transients described above. At long times (after about $t \sim 4 \times 10^3 GM/c^3 \approx 70 T_{\text{isco}}$) the behavior of these simulations begins to deviate. HD2d_1 continues to decay in an approximately exponential manner $K(t) \propto e^{-t/\tau_0}$, where $\tau_0 \approx 4 \times 10^3 GM/c^3$. Superposed on this decay is a distinct oscillation. This corresponds to (twice) the frequency of the trapped g -mode that we shall discuss below. The high-resolution version of this simulation HD2d_1hr shows very similar behavior except that the exponential decay time is longer, $\tau_0 \approx 6 \times 10^3 GM/c^3$. This suggests that the decay of these small perturbations is due to numerical dissipation, which approximately scales as the square root of the size of the simulation grid cells.

We now study the spatio-temporal variability of the disk and, in particular, seek the diskoseismic modes predicted by linear theory. Figure 3 shows the midplane value of v_r on the (r, t) -plane, that is, the value of the function $v_r(r, z = 0; t)$, for run HD2d_1. Note that, outside of the ISCO, the average value is $\langle v_r \rangle \ll 0.001c$ so that this figure essentially plots the fluctuation of v_r from its mean value. At early times, we see strong wave-like disturbances that are generated in the inner parts of the disk (at $r \approx 8r_g$) and propagate to both large and small radii. Although the outer radial boundary condition is a zero-gradient outflow, impedance mismatching results in some reflection of these initial strong waves. After these initial transients have died out, it can be seen that the highest amplitude fluctuations are limited to a rather narrow range of radii in the approximate range $r=7-9r_g$. The fact that these perturbations are essentially vertical on the (t, r) -plane indicates that they are coherent across this radial range, as would be expected if we see a global mode.

This temporal variability can be explored in more detail using the power spectral density (PSD), defined as $P(v) = \alpha |\hat{f}(v)|^2$,

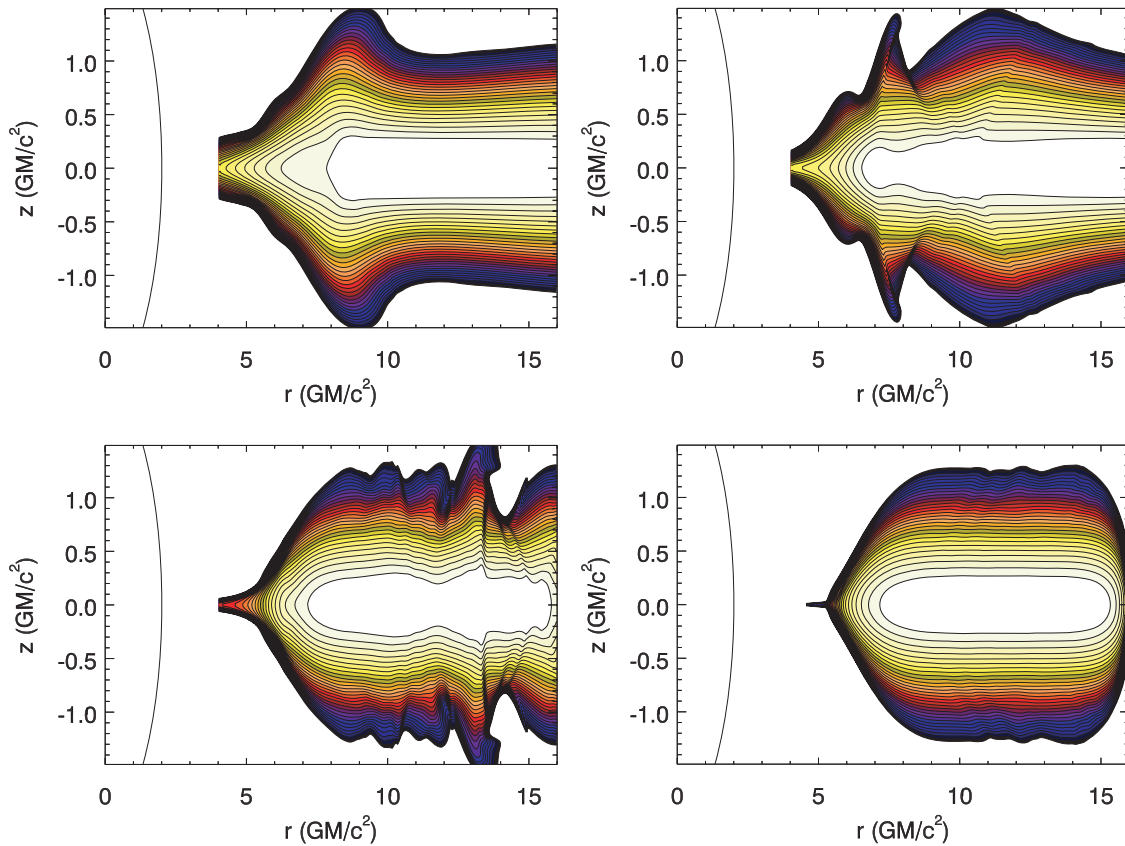


Figure 1. Snapshots of evolution of the canonical axisymmetric hydrodynamic simulation (HD2d_1) at $t = 0.5T_{\text{isco}}$ (top-left), $t = 1.0T_{\text{isco}}$ (top-right), $t = 5T_{\text{isco}}$ (bottom-left), and $t = 50T_{\text{isco}}$ (bottom-right), where T_{isco} is the orbital period at the ISCO. Both the color table and contours show the logarithmic density structure of the disk cross section, with 10 contours per decade of density. A range of densities spanning three orders of magnitude are shown. The curved line to the left of each frame represents the event horizon.

(A color version of this figure is available in the online journal.)

where α is some normalization constant and $\tilde{f}(\nu)$ is the Fourier transform (FT) of the time sequence $f(t)$ under consideration:

$$\tilde{f}(\nu) = \int f(t)e^{-2\pi i\nu t} dt. \quad (17)$$

Note that, for ease of interpretation, most of the PSDs presented in this paper will be in terms of the usual frequency, ν , rather than the angular frequency, ω . Figure 4 shows the PSD of the midplane pressure as a function of r and frequency for HD2d_1 and HD2d_1hr. This is computed using approximately the final half ($\Delta t = 102.4T_{\text{isco}} \approx 6308 GM/c^3$) of the simulation in order to avoid the initial strong transients. These PSDs differ in the range $r = 12 - 16r_g$; run HD2d_1hr has significantly less low-frequency noise than run HD2d_1 in this radial range. We attribute this to effects related to the outer radial boundary, which is at $r = 16r_g$ in run HD2d_1 but substantially further out ($r = 28r_g$) in run HD2d_1hr.

Inside of $r = 12r_g$, however, the PSDs of these two simulations are very similar and we can trust that neither the resolution nor the outer radial boundary affects the results significantly. We note that simulations in which the initial radial density profile of the disk is truncated before reaching the outer boundary also produce essentially identical results, again giving us confidence that noise infiltration from the outer boundary is not an important issue. In addition to very low frequency noise, the most prominent feature of the inner-disk PSD is a vertical ridge of enhanced power at $\nu \approx (4-5) \times 10^{-3} c^3/GM$ extending from $r \approx 6.5r_g$ out to $r \approx 9.5r_g$. The one-dimensional cuts

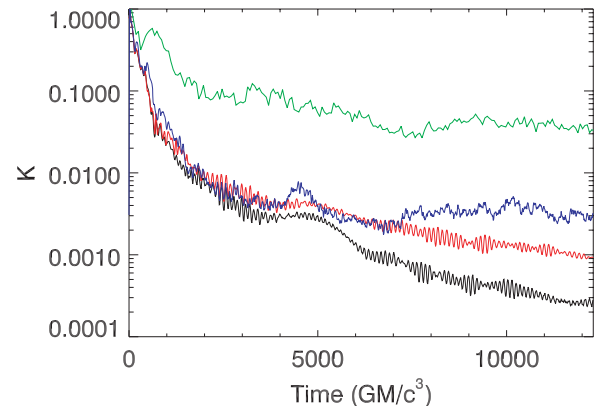


Figure 2. Change of the quantity $K = \int_{\mathcal{D}} \rho v_z^2 dV$ with time. The integration domain \mathcal{D} is the annulus $r \in (7, 14)$. The bottom (black) line is for the canonical two-dimensional run (HD2d_1), lower-middle (red) line is for the high-resolution two-dimensional run (HD2d_1hr), the upper-middle (blue) line is for the canonical three-dimensional run (HD3d_1), and the top (green) line is for the canonical MHD run (MHD_1). The distinct “ringing” seen in runs HD2d_1 and HD2d_1hr corresponds to the axisymmetric g -mode (see Section 3.3). In run HD3d_1, nonaxisymmetric aperiodic structures mask the underlying g -mode (see Section 3.4). The fact that $K(t)$ for the run MHD_1 lies an order of magnitude above that for HD3d_1 demonstrates that the MRI-driven turbulence completely overwhelms the hydrodynamic disturbances seen in the analogous three-dimensional hydrodynamic simulation (see Section 4.2).

(A color version of this figure is available in the online journal.)

through this ridge in Figure 5 demonstrate it to have all of the expected properties of a trapped g -mode. First, it exists in a

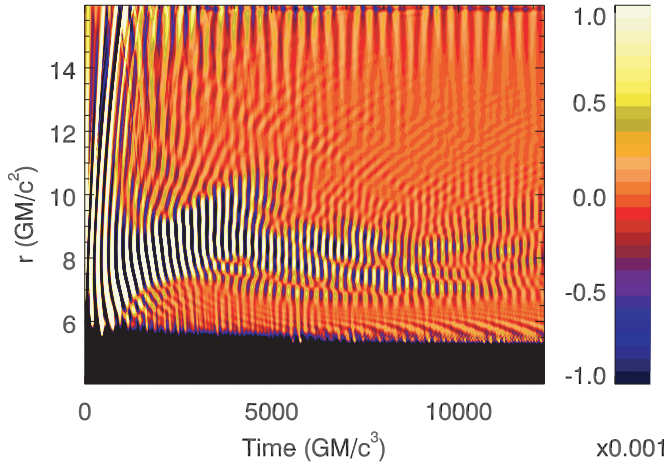


Figure 3. Radial component of velocity v_r on the midplane of the disk as a function of radius and time for the canonical axisymmetric hydrodynamic simulation (HD2d_1). The linear color table extends from radial velocities of $v_r = -0.001c$ (black) to $v_r = +0.001c$ (white). Note that, outside of the ISCO, the average value is $|v_r| \ll 0.001c$ so that this diagram essentially plots the fluctuation of v_r from its mean value.

(A color version of this figure is available in the online journal.)

rather narrow range of frequencies, $\nu \approx (4-5) \times 10^{-3} c^3/GM$, just below the maximum radial epicyclic frequency ($\kappa_{\max} \approx 5.52 \times 10^{-3} c^3/GM$). Second, it is spatially bounded by the radii at which the mode frequency becomes equal to the radial epicyclic frequency. There is, however, some leaking of the mode down to the ISCO.

We can visualize the eigenmode by producing maps of pressure deviations that have been “period-folded” on the period corresponding to the peak power in this mode. More precisely, we use the last half of the simulation to produce maps of the difference between the instantaneous pressure and the time-averaged pressure with a sampling rate of $0.2T_{\text{ISCO}}$. We then sort these maps into 16 phase bins (based on the period corresponding to the peak power in this mode) and average together all maps within a given phase bin. The result is shown in Figure 6. In addition to the g -mode itself, these maps reveal a striking “chevron” pattern at large radii. Time sequences of maps reveal these features to be outward-radially traveling acoustic

waves driven by the global g -mode, refracted into the upper layers of the disk atmosphere as they propagate.

As a final demonstration that we have properly identified trapped g -modes in our axisymmetric hydrodynamic simulations, we use our set of runs to study the dependence of the mode frequency on the sound speed in the disk. Figure 7 shows the dependence of the mode frequency on the midplane sound speed of the disk (and, hence, disk thickness) at $r = 8r_g$. As expected from analytical theory (see Appendix A), the difference between the mode frequency and the maximum epicyclic frequency linearly depends on the sound speed. There is, however, a discrepancy in the slope of this linear relationship obtained by the simulations and expected from the analytical theory. Note that the analytical treatment assumes that the gas is strictly isothermal across the whole region of interest, a condition that is clearly violated in the simulated disk. Given the sensitivity of the mode to the radial structure of the disk (as demonstrated by the factor of 2.5 difference in the analytical results between the two pseudo-Newtonian potentials examined in Appendix A), the nonisothermality of the gas in the simulated disk can readily shift the mode frequency away from the analytical value.

3.4. Extension to Three-Dimensional Hydrodynamic Models

We begin our analysis of the three-dimensional hydrodynamic simulations (HD3d_1) by examining the decay of hydrodynamic perturbations in our canonical three-dimensional run (HD3d_1) using the quantity $K(t)$ as defined in Equation (16). The $K(t)$ behavior for HD3d_1 is somewhat different from the axisymmetric simulations at late times, reaching a quasi-steady state at $K/\max(K) \sim 3 \times 10^{-3}$ with aperiodic fluctuations rather than continuing a ringing exponential decay (Figure 2). Numerical dissipation must be just as effective in HD3d_1 as compared with HD2d_1; hence, these perturbations must be driven by some instability. While it is thought that free Keplerian accretion disks are stable to linear hydrodynamic perturbations (see Balbus & Hawley 1998; Hantao et al. 2006), the presence of the simulation boundaries can introduce true instabilities (associated with reflection from the boundaries) and uncontrolled numerical noise, and these might explain these low-level sustained fluctuations. Visual inspection of density slices in the (r, z) - and (r, ϕ) -planes also suggests that nonaxisymmetric wavelike perturbations interacting with the

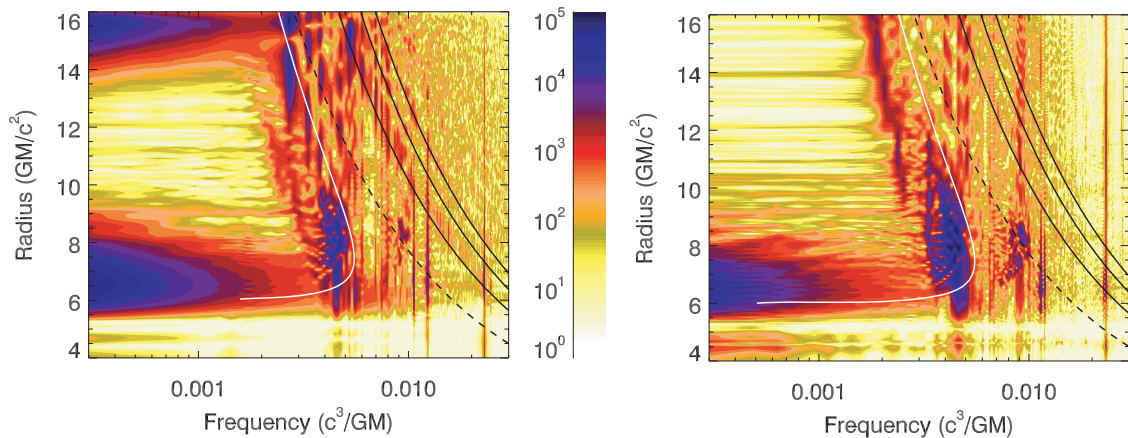


Figure 4. Midplane PSD for pressure fluctuations in run HD2d_1 (left panel) and its high-resolution counterpart HD2d_1hr (right panel). Note that we show the radial range $r \in (4, 16)$, which is coincident with the full computational domain of HD2d_1 but only the inner half of the domain for HD2d_1hr (whose full radial domain extends from $4r_g$ to $28r_g$). Also shown are the radial epicyclic frequency (solid white line), orbital frequency (dashed), and the $n = 1, 2, 3$ pure vertical p -modes (from left to right dot-dashed lines). The absolute scaling of the PSD, as indicated by the color bar, is arbitrary.

(A color version of this figure is available in the online journal.)

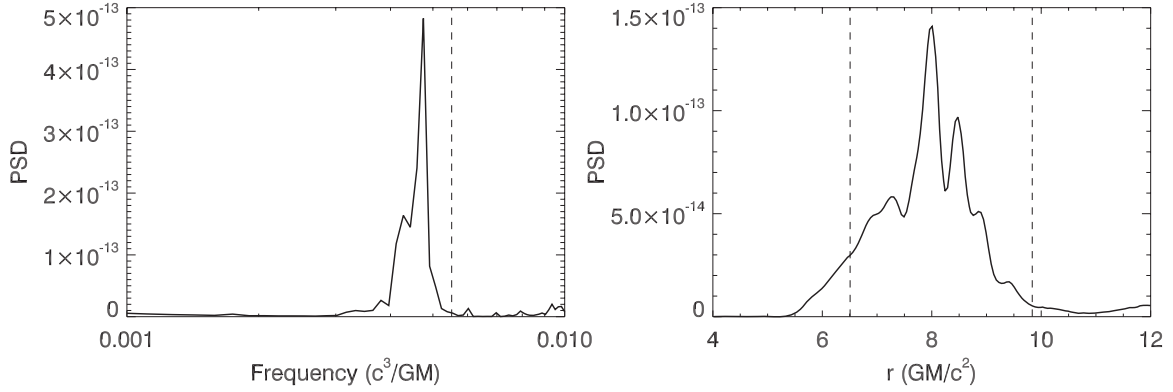


Figure 5. Left panel: midplane pressure PSD for run HD2d_1 summed up over a range of radii $\Delta r = 0.5r_g$ centered on $r = 8r_g$. The dashed line shows the maximum radial epicyclic frequency. Right panel: integral of the midplane pressure PSD of those frequency bins that exceed 5×10^{-14} in the left panel, as a function of radius. Vertical dashed lines show the range of radii for which the mean frequency of this peak is less than the radial epicyclic frequency.

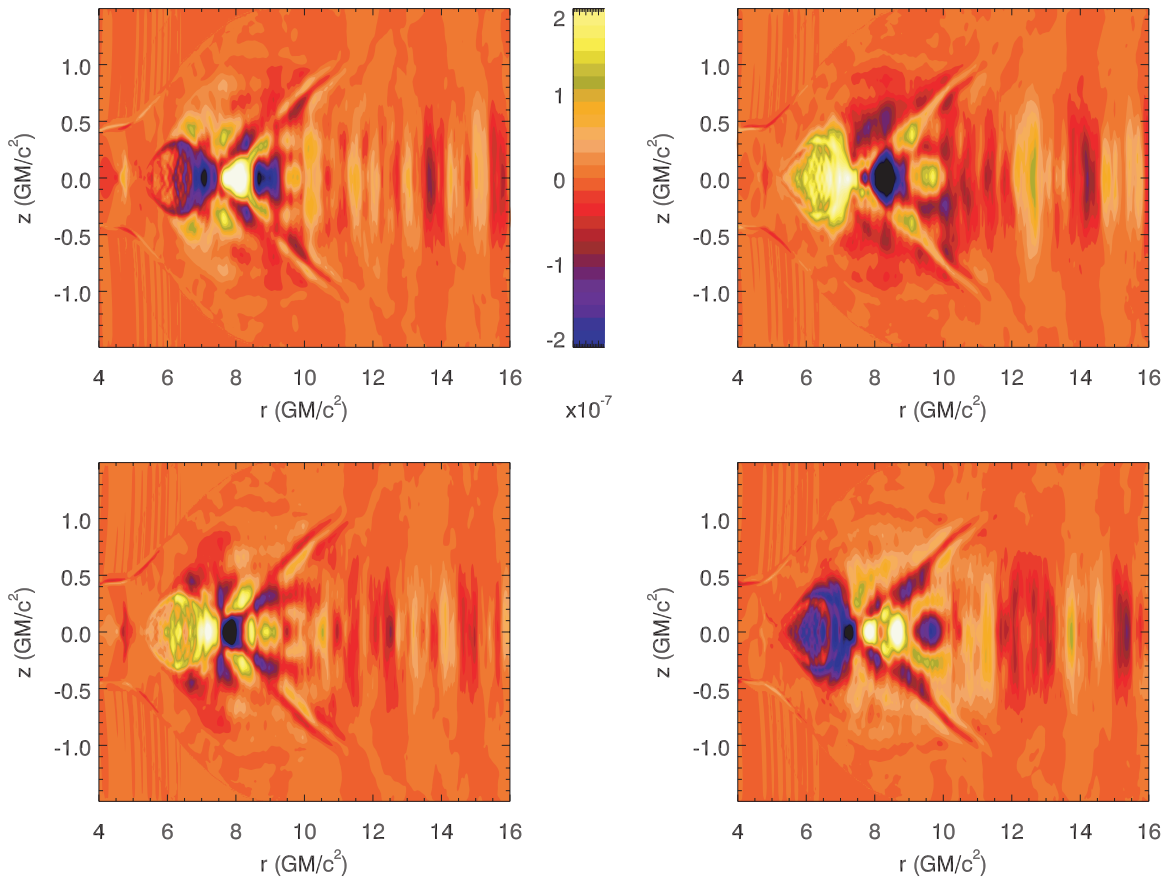


Figure 6. Maps of period-folded pressure deviation (i.e., the difference between the instantaneous pressure and the time-averaged pressure) for run HD2d_1hr. Only the last 102.4 orbits of data have been included in order to avoid the transient behavior associated with the initial conditions. The folding period corresponds to the peak of the PSD seen in Figure 5. Phases of 0.0 (top left), 0.25 (top right), 0.5 (bottom left), and 0.75 (bottom right) are shown. This, in essence, gives us a direct view of the eigenmode.

(A color version of this figure is available in the online journal.)

boundaries are responsible for perturbing the three-dimensional hydrodynamic disk. However, a detailed study of the sustained fluctuations in the three-dimensional hydrodynamic disks is beyond the scope of this paper. Since these perturbations exist at a low level (particularly compared with the MHD turbulence discussed in Section 4; see Figure 2 for a comparison of the sustained fluctuations in the three-dimensional hydrodynamic run compared with the canonical MHD run) and are likely to be driven by our boundaries (hence, are not of astrophysical

relevance), they are not of importance for the principal focus of our study.

The principal issue to be addressed here is the impact of the transition to three dimensions on the presence of the trapped $m = 0$ g -modes in the simulated disks. We might expect the power in these axisymmetric modes to be reduced in the three-dimensional case as the free energy is shared with nonaxisymmetric modes. This is indeed the case. Figure 8 shows the PSD at $r = 8r_g$ of the last $\Delta t = 102.4T_{\text{ischo}}$ of the

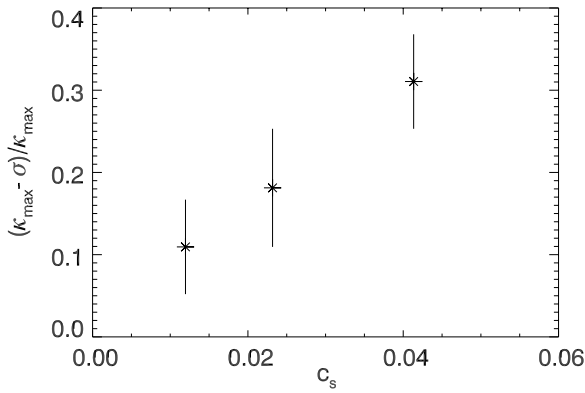


Figure 7. Frequency of the g -modes as a function of midplane sound speed at $r = 8r_g$ for runs HD2d_2, HD2d_1, and HD2d_3 (from left to right). The vertical bars indicate the range of frequencies over which enhanced power is seen.

canonical three-dimensional run HD3d_1. A region of enhanced power is clearly seen in the correct range of frequencies $\nu \approx (4 - 5) \times 10^{-3} c^3/GM$ to be identified with the axisymmetric g -modes studied in Section 3.3. Furthermore, examination of the radially resolved PSD shows that this region of enhanced power is bounded by the radial epicyclic frequency in precisely the manner expected for trapped g -modes. A comparison of the absolute values of the PSD across the mode does reveal, however, that the mode contains almost an order-of-magnitude less power than in the axisymmetric case.

We note the existence of a narrow but large amplitude spike just above a frequency of $7 \times 10^{-3} c^3/GM$ in the $r = 8r_g$ PSD of this run. The identification of this feature is not clear; it is not at the frequency of any expected global g - or p -mode. It is, however, confined to a single frequency bin, contains only a small amount of power, and only shows up over a narrow range of radii. It seems likely that this is a noise spike.

4. MAGNETOHYDRODYNAMIC DISKS

Having gained an understanding of the thin hydrodynamic disks, we move onto the more astrophysically relevant case of MHD disks. In this section, we construct MHD simulations of thin accretion disks in a PW potential. We then examine the properties of the broadband noise and search for modes in the resulting turbulent MHD disks.

4.1. Simulation Setup

We simulate geometrically thin MHD accretion disks by building upon our hydrodynamic computational setup described in Section 3.2. As discussed in Section 3.1, we only consider three-dimensional MHD simulations.

Table 1 details our set of MHD simulations. Most of our discussion will center around run MHD_1 (which we shall refer to as our canonical MHD run). In this run, the hydrodynamic variables are setup as for the canonical hydrodynamic run (see Section 3.2) except that we begin the disk in vertical hydrostatic equilibrium ($h_1 = h_2 = 0.3r_g$ corresponding to $h_1/r = h_2/r = 0.05$ at the ISCO). An initially weak magnetic field is introduced in the form of poloidal field loops specified in terms of their vector potential $\mathbf{A} = (A_r, A_z, A_\phi)$ in order to ensure that the initial field is divergence free. We choose the explicit form for the vector potential,

$$A_\phi = A_0 f(r, z) p^{1/2} \sin\left(\frac{2\pi r}{5h_1}\right), \quad A_r = A_z = 0, \quad (18)$$

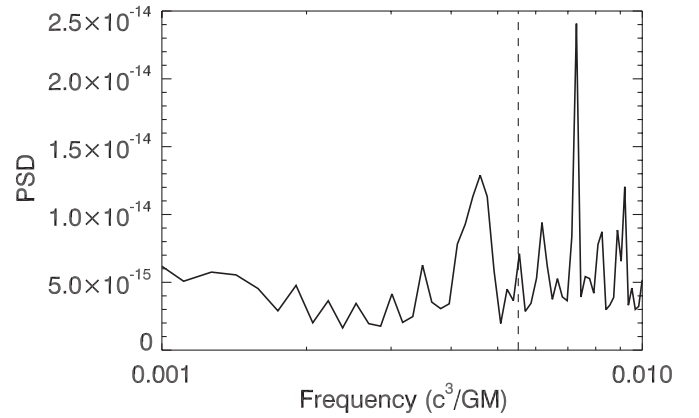


Figure 8. Midplane PSD of azimuthally averaged pressure for run HD3d_1 summed up over a range of radii $\Delta r = 0.5r_g$ centered on $r = 8r_g$. The dashed line shows the maximum epicyclic frequency.

where A_0 is a normalization constant and $f(r, z)$ is an envelope function that is unity in the body of the disk and then smoothly goes to zero at $r = r_{\text{isco}}, r = r_{\text{out}}$, and at a location three pressure scale heights away from the midplane of the disk. The use of $f(r, z)$ keeps the initial field configuration well away from either the radial boundaries of the initial disk configuration or the vertical boundaries of the calculation domain. The final multiplicative term produces field reversals with a radial wavelength of $5h$. This results in a number of distinct poloidal loops throughout the disk. The normalization constant A_0 is set to give an initial ratio of gas-to-magnetic pressure of $\beta = 10^3$ in the inner disk. In our canonical MHD simulation, this initial condition is evolved for a duration of $630T_{\text{isco}}$ ($38800 GM/c^3$) using the MPI-parallelized version of ZEUS described above.

We supplement the ideal MHD algorithms of ZEUS in two ways. First, it is necessary to impose a floor on the density field of 10^{-5} times the initial maximum density in order to prevent the numerical integration from producing negative densities. This essentially amounts to a subtle distributed mass source. The density only reaches this floor close to the z -boundary (i.e., many scale heights above and below the disk plane). Second, we implement the prescription of Miller & Stone (2000) to include some effects of the displacement current, principally forcing the Alfvén speed to correctly limit to the speed of light as the magnetic fields become strong. We note that this “Alfvén speed limiter” only plays a role within small patches of the tenuous magnetized atmosphere that forms at large vertical distances above and below the disk; it never plays a significant role in the body of the accretion disk.

Periodic boundary conditions were imposed on the ϕ -boundaries, and zero-gradient outflow boundary conditions were imposed at both the inner and outer radial boundaries (Stone & Norman 1992a, 1992b). However, the choice of the z -boundary condition for this kind of simulation is notoriously problematic. The most physically motivated choice would be a free outflow boundary. However, as described in Stone et al. (1996), field-line “snapping” at these free boundaries can halt such a simulation. Indeed, our own test simulations employing zero-gradient outflow boundary conditions on the z -boundaries were found to be subject to these difficulties, as well as occasional numerical instabilities appearing to result from an interplay of the imposition of the density floor and the free boundary. Furthermore, these tests showed that the tenuous matter high above the disk midplane generally flows slowly across these boundaries at very subsonic and sub-Alfvénic speeds; strictly,

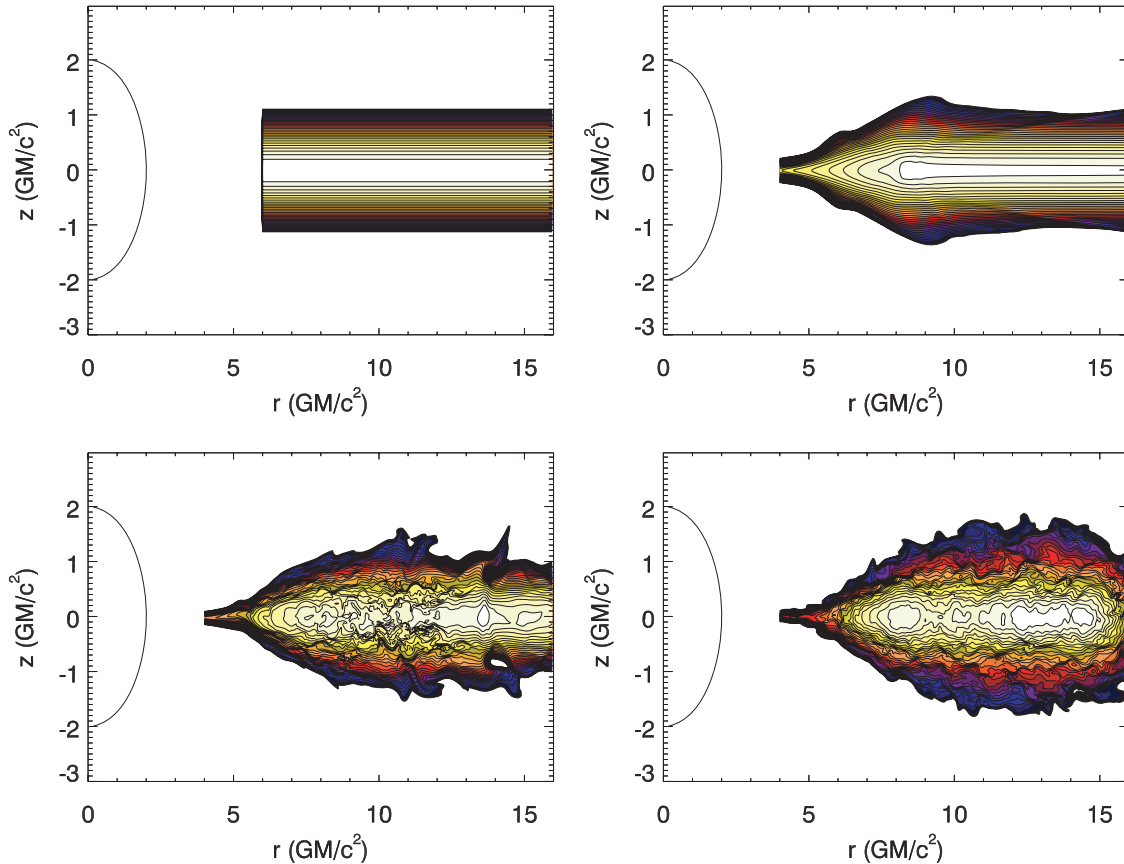


Figure 9. Snapshots of evolution of the canonical MHD simulation (MHD_1) at $t = 0$ (top left), $t = 17T_{\text{isco}}$ (top right), $t = 10T_{\text{isco}}$ (bottom left) and $t = 100T_{\text{isco}}$ (bottom right), where T_{isco} is the orbital period at the ISCO. Both the color table and contours show the logarithmic density structure of the disk cross section, with 10 contours per decade of density. A range of densities spanning 3 orders of magnitude are shown. The curved line to the left of each frame represents the event horizon. (A color version of this figure is available in the online journal.)

this anyways invalidates the use of such boundary conditions (since the flow on the other side of the boundary should be able to act back on the simulation domain).

We adopt the solution of Stone et al. (1996) and choose to employ periodic boundary conditions in the z -directions. While this is obviously unphysical in the sense that matter cannot leave the simulation domain in the vertical direction, it does guarantee mathematically reasonable behavior at the boundary (eliminating numerical instabilities) and, more importantly, appears to have no effect on the dynamics of the accretion disk itself (as diagnosed through comparisons with our vertical-outflow test runs). In order to further isolate the simulated disk from the vertical boundaries, we expand the vertical domain (compared with the canonical hydrodynamic simulation) to $z \in (-3, 3)$ (i.e., $\pm 10h_1$).

We perform four additional simulations aimed at demonstrating the robustness of the canonical simulation. In run MHD_2, we restrict the vertical domain back to $z \in (-1.5, 1.5)$, allowing us to gauge the importance of the location of the z -boundaries. Run MHD_2hr has a setup identical to MHD_2 except that the radial and vertical resolutions are doubled compared with the canonical run (i.e., the voxel size is reduced by a factor of 2 in each of the radial and vertical directions), and the azimuthal domain is doubled to $\Delta\phi = 60^\circ$ at fixed resolution. Due to the factor of 8 increase in the number of computational cells (and the decrease in the timestep), this run was only integrated for a duration of $85T_{\text{isco}}$ ($5236 GM/c^3$). While the run time is insufficient to conduct a detailed temporal study, a comparison with

run MHD_2 does allow us to investigate the effect of both the radial/vertical resolution and the extent of the ϕ -domain on the turbulent state (see below). As discussed below, we find that the properties of the simulated disks are very similar to these two runs.

Run MHD_3 is similar to MHD_2 except that the outer radius is pushed to $r = 28r_g$ (at fixed resolution), doubling the size of the radial domain. Comparing MHD_2 with MHD_3, we find no evidence that the outer radial boundary affects the inner disk ($r < 12r_g$) in any way.

4.2. Basic Evolution of the MHD Disks

We now discuss the evolution and general properties of these MHD disks, centering our discussion around run MHD_1. At very early times ($t < 5T_{\text{isco}}$), strong hydrodynamic transients dominate the evolution as radial pressure forces drive mass into the region within the ISCO. Similar to the hydrodynamic cases, these transients launch outwardly directed axisymmetric waves that break to form rolls. These strong hydrodynamic transients largely damp away in all but the outermost parts of the disk within $10T_{\text{isco}}$. Concurrently, the MRI amplifies the initial magnetic field until the (domain wide) volume-averaged ratio of gas-to-magnetic pressure peaks at $\langle\beta\rangle \sim 5$ (at $t \approx 10T_{\text{isco}}$), at which point most of the flow has become turbulent. The entire flow (outside of the ISCO) becomes turbulent by $t \approx 20T_{\text{isco}}$. Figure 9 displays the density field across a vertical slice through the accretion disk at various times.

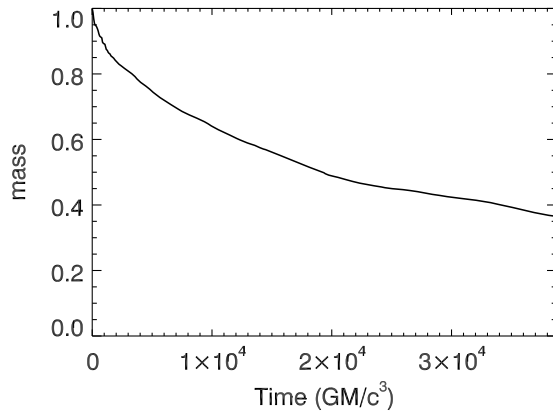


Figure 10. Normalized total mass as a function of time for run MHD_1.

Between $t = 10T_{\text{isco}}$ and $t = 20T_{\text{isco}}$, the total magnetic energy in the computational domain declines until $\langle\beta\rangle \sim 20$. After this, a quasi-steady state seems to be achieved where the magnetic field generation by the MRI-driven MHD turbulence is balanced by the removal of magnetic field energy due to numerical reconnection and magnetic buoyancy. The fact that buoyancy is playing an important role is revealed by examining time sequences of the strengths of B-field components in (r, z) cross-sections of the disk. One clearly sees highly magnetized structures being generated close to the midplane of the disk, which then propagate vertically away from the midplane.² From this time until the end of the simulation at $t = 630T_{\text{isco}}$, MHD turbulence and hence accretion is sustained. Over the course of the simulation, the disk loses a little more than 60% of its mass (Figure 10).

The total magnetic energy and thermal energy undergo a slow decline as mass is drained out of the simulated disk. During this decline, the volume-averaged plasma- β parameter within the domain remains in the range $\langle\beta\rangle \sim 20\text{--}30$. However, as expected, the β parameter within the high-density body of the disk is appreciably higher, reaching values of $\beta \approx 70\text{--}100$.

² In principle, one could address the importance of magnetic buoyancy in removing magnetic energy from the midplane regions of the disk by comparing the vertical Poynting flux with (numerical) reconnection losses. However, energy losses due to numerical reconnection cannot be tracked in our simulation (due to the nonconservative nature of the ZEUS algorithm) and, hence, a rigorous study of this issue is not possible.

While this is significantly larger than the β found in global simulations of thicker disks (e.g., Hawley & Krolik 2001, 2002), it is in line with what might be expected for thin accretion disks with a zero net field as diagnosed through local shearing-box simulations both with and without vertical stratification (Stone et al. 1996; Hawley et al. 1996; Miller & Stone 2000).

A generic concern in this class of simulation is the effect of the z -boundaries. Once it achieves its quasi-steady state, our canonical MHD simulation displays a 2–3 order-of-magnitude drop in magnetic pressure, and a 5 order-of-magnitude drop in gas pressure, between the disk and the z -boundary. Thus, the disk boundary seems to be well isolated from the boundary. Further confidence is gained from an examination of run MHD_2 in which the z -boundaries have been brought in from $z = \pm 3$ to $z = \pm 1.5$. Despite the fact that the magnetic pressure now only drops by 1 order of magnitude from the disk to the boundary, all of the results from the canonical MHD run discussed in this paper are reproduced by MHD_2. More precisely, (1) the PSD of the fluid variables (Section 4.3.2) are essentially indistinguishable, failing to show any evidence of global modes but displaying prominent local p -modes, (2) the PSD of the mass accretion rate has a broken power-law form with indices that differ from those found in MHD_1 by $\Delta\gamma \approx 0.1$ (comparable with the 1σ error bars) and break frequencies that differ by $\Delta(\log \nu_{\text{break}}) \approx 0.05$ (again, comparable with the 1σ error bars).

Another generic concern with thin disk simulations is whether the resolution in the vertical direction is adequate. The canonical MHD simulation (MHD_1) has approximately 13 grid cells spanning a vertical range $\Delta z = h_2$, implying that we cannot follow any modes with a wavelength smaller than $\lambda \sim h_2/2$. This is just sufficient to follow the fastest growing MRI mode (with wavelength $\lambda \sim 2\pi h/\beta^{1/2}$) if $\beta \lesssim 100$. To ensure that we have, in fact, achieved adequate resolution, we compare run MHD_2 and its high resolution counterpart, run MHD_2hr. For example, Figure 11 compares the time dependence of the thermal and magnetic energies, as well as the height dependence of the plasma- β parameter. While there is some indication of increased buoyancy-driven escape of magnetic fields from the high-resolution simulation (as is apparent from the higher value of β at intermediate heights), the two simulations generally compare very well. Thus, we conclude that we have achieved adequate numerical resolution.

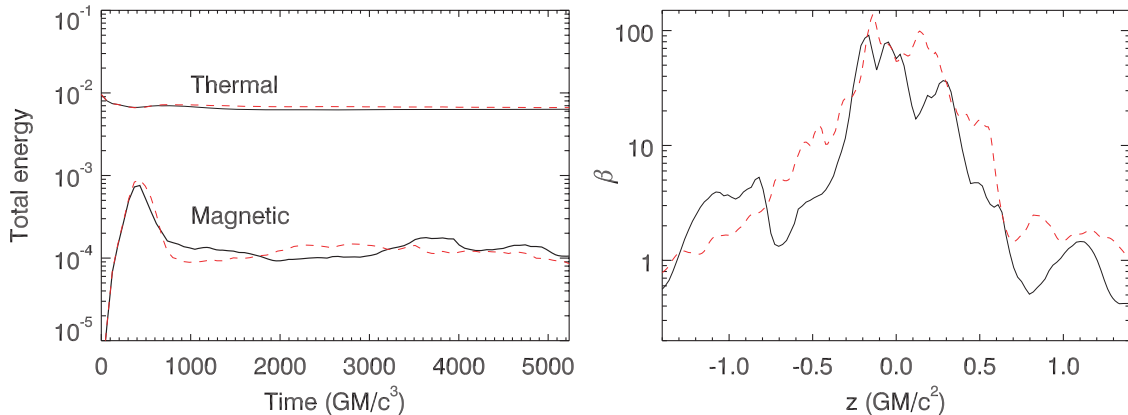


Figure 11. Left panel: total (domain integrated) magnetic and thermal energies for run MHD_2 (black solid line) and its high-resolution counterpart (MHD_2hr; red dashed line). Right panel: azimuthally averaged plasma- β parameter (i.e., the ratio of the thermal-to-magnetic pressure) as a function of vertical height in the disk at $r = 8r_g$. To obtain this plot, data from $t = 30 - 35T_{\text{isco}}$ have been averaged together. The solid (black) line shows run MHD_2 whereas the dashed (red) line shows its high-resolution counterpart (MHD_2hr).

(A color version of this figure is available in the online journal.)

4.3. Temporal Power Spectra of the Basic Fluid Variables

4.3.1. The Importance of Correcting for Secular Changes During the Simulation

The length of our canonical MHD run makes it well suited for a detailed study of temporal variability. In particular, the long stream of simulation data facilitates the construction of PSDs. However, as we now discuss, significant complications arise in the analysis of these MHD simulations as compared with the pure hydrodynamic simulations.

In the case of the hydrodynamic simulations, the background (i.e., unperturbed) flow achieves almost a stationary state once the large transients caused by the initial conditions have died out. In particular, the lack of angular momentum transport within the hydrodynamic disk (other than that due to the very small numerical viscosity) allows the disk to achieve a nonaccreting state. Density and pressure fluctuations about this background state can then be studied via the straightforward construction of the PSD. The constant background level does not contribute to the power spectrum and, hence, the PSD faithfully characterizes the fluctuations of interest.

However, even once the initial transients have been dissipated, MHD disks never achieve this kind of stationary background flow. MHD turbulence leads to continued accretion that depletes mass from the simulated disks. This decline in total mass leads to secular changes (with an approximately exponential form) in the density and pressure of the background flow. Unless corrected for, even a rather slow exponential decay can have a significant influence on the PSD of the pressure or density fluctuations, severely affecting attempts to characterize the properties of the astrophysically relevant fluctuations (i.e., the fluctuations that would be present in the ideal case of a steady-state disk in which the mass was replaced from a large reservoir).

To see this, consider some quantity whose time series $f(t)$ we extract from the simulation (e.g., this could be the midplane density or pressure at some given radius). Let us assume that this can be decomposed as

$$f(t) = \epsilon(t)[1 + g(t)], \quad (19)$$

where $g(t)$ is the time series of the astrophysically interesting fluctuations about some mean state (i.e., $\langle g \rangle = 0$) and $\epsilon(t)$ is a decay function that describes the secular change in the background state due to the draining of mass from the simulation. It must be noted that the decomposition given in Equation (19) is not completely general; this assumes that the amplitude of the “real” fluctuations is proportional to the mean background value, and that the properties of the fluctuations otherwise remain invariant as the background state decays. This decomposition would be valid if the decay of the simulated disk simply amounted to a gradual decline in the density scale of the simulation while the temperature and velocity structures remained unchanged. We shall refer to such (simulated) disks as *density-invariant disks*. This does indeed appear to describe our simulated MHD disks (i.e., there is little or no corresponding secular change in disk thickness or characteristic turbulent velocities). In this case, the mass accretion rate will be proportional to the density and the decay will hence have an exponential form, $\epsilon = \epsilon_0 e^{-t/t_0}$.

In the uninteresting case where there are no fluctuations ($g(t) = 0, \forall t$), the observed signal is just $f(t) = \epsilon(t)$, leading to a FT and PSD given by

$$\tilde{\epsilon}(\omega) = \frac{A_1}{(1/t_0) + i\omega} \quad \text{and} \quad P_\epsilon(\omega) = \frac{A_2}{(1/t_0)^2 + \omega^2}, \quad (20)$$

where A_1 and A_2 are uninteresting normalization constants. Thus, for $\omega \gg 1/t_0$, the PSD of the exponential decay goes as $P_\epsilon(\omega) \propto \omega^{-2}$.

In the more interesting case of nonzero fluctuations, the FT of the observed signal is

$$\tilde{f}(\omega) = \tilde{\epsilon}(\omega) + \int \tilde{\epsilon}(\omega') \tilde{g}(\omega - \omega') d\omega', \quad (21)$$

that is, the sum of the FT of the exponential decay with the convolution of the FTs of the decay and the interesting fluctuations. When the fluctuations are small compared with the (decaying) background state, as is the case for the density and pressure, one can see that the PSD of the observed signal will be dominated by $1/\omega^2$ associated with the decay. Even in the case where the fluctuations are large compared with the decay, the PSD will still be influenced by the exponential decay due to the convolution term in Equation (21). In particular, regions of the “real” PSD that are steeper than ω^{-2} (including the high-frequency wing of any QPO or regions above a high-frequency break) will tend to get filled.

Clearly, we must correct for this decay of the background state, and be cognizant of manifestations of any remaining uncorrected effects of this decay. This procedure plays the same role as the “prewhitening” employed by Schnittman et al. (2006; hereafter SKH). We proceed by dividing the observed time series by a “best-fitting” exponential decay function. Here, the time constant of the exponential decay t_0 is estimated via two methods. First, we can set t_0 by the requirement that the starting and final values of the observed series are equal ($f(t=0) = f(t=T)$, where $t=T$ corresponds to the end of the time series). This is the procedure adopted by SKH except that they employed a linear form for the decay function. Secondly, we can set t_0 via a least-square fit of an exponential form to the observed time series. These methods give very similar values of t_0 and similar corrected PSDs when applied to density or pressure fluctuations, as we shall now see.

4.3.2. Power Spectra of Fluid Variables in Disk Midplane

We now examine the PSD of the azimuthally averaged fluid variables (velocities, pressure, and density) for the simulated MHD disks, as we did with the hydrodynamic disks in Section 3.3. The top panels of Figure 12 show the PSD for the radial and vertical components of velocity in the midplane of the disk, $v_r^{\text{mid}}(r, t)$ and $v_z^{\text{mid}}(r, t)$, respectively, for a duration lasting $\Delta t = 409.6T_{\text{isco}}$ starting at $t = 100T_{\text{isco}}$ (i.e., well after all of the initial transients have dissipated and a quasi-steady turbulent state has been established). Note that, outside of the ISCO, these velocity components are themselves first-order fluctuating quantities (i.e., the radial and vertical velocities of the background state are approximately zero) and, within the density-invariant disk assumption, will have characteristic fluctuation amplitudes that remain constant throughout the simulation. Hence, we do not need to correct these PSDs for the effect of the density decay in the simulation.

It is readily seen that the PSD of the midplane radial velocity v_r^{mid} is dominated by the radial epicyclic frequency from $r \sim 7-8r_g$ out to the outer radial boundary. Inside of $r \approx 7-8r_g$, the PSD shows broadband power associated with the transition from turbulent to plunging flow.

The PSD of the midplane vertical velocity v_z^{mid} is quite different and can be interpreted in the light of the *local* fluid oscillations discussed in Section 2.1. Below the radial epicyclic

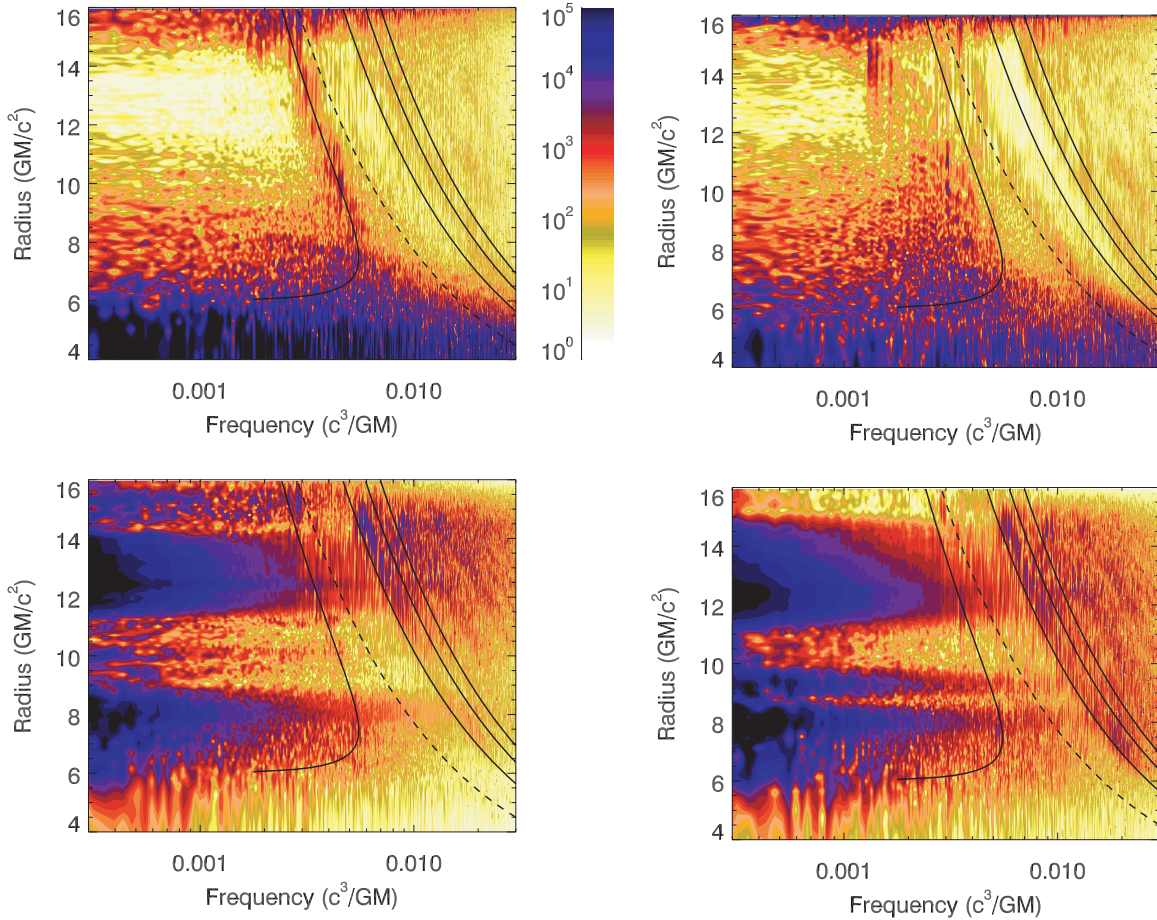


Figure 12. PSD for azimuthally averaged midplane fluid quantities from run MHD_1. Panels show PSDs for radial velocity (top left), vertical velocity (top right), density (bottom left), and pressure (bottom right). The density and pressure variables have been divided by the least-square best-fitting exponential function to correct for the secular decay of the simulation, as discussed in Section 4.3.1. Also shown are the radial epicyclic frequency (solid), orbital frequency (dashed), and the $n = 1, 2, 3$ pure vertical p -modes (from left to right dot-dashed lines). The absolute scaling of the PSDs, as indicated by the color bar, is arbitrary.

(A color version of this figure is available in the online journal.)

frequency, there is a broad spectrum of g -modes. Above the orbital frequency, the distinct modes described by Equation (4) become apparent; the $n = 0$ mode ($\omega > \Omega$) and $n = 2$ mode ($\omega > 2.08\Omega$) can be picked out as distinct tracks, and there are hints of higher frequency modes as well. The fact that only even- n modes are seen is readily understood given that the odd- n modes have v_z -nodes at the midplane, as is evident from the power deficit centered on the $n = 1$ frequency in the v_z PSD.

The bottom panels of Figure 12 show the corresponding PSD for the density and pressure from the canonical simulation. The displayed PSDs have been corrected for the decay of the background state by dividing through by an exponential curve that best fits (in a least-square sense) the domain-averaged density or pressure. Very similar results are obtained using an exponential determined from just the end points. The radial banding of the low-frequency noise is largely the effect of the prewhitening procedure; the full (noncorrected) low-frequency power is somewhat greater, and the bands correspond to the residuals between the real decay and the simple exponential model. In addition to this low-frequency noise (which is of secondary interest to the investigation presented in this paper), both PSDs show an enhancement corresponding to the $n = 1$ vertical p -mode (with $\omega > 1.63\Omega$). As expected, there is no enhancement in the density or pressure PSDs corresponding to the $n = 0$ or $n = 2$ p -modes; these have pressure and density nodes at the midplane.

In stark contrast to the hydrodynamic simulation, the (decay-corrected) midplane pressure PSD does not show the κ -bounded vertical “ridge” on the frequency–radius plane that is characteristic of trapped g -modes. The absence of an excited trapped g -mode is also confirmed by examining the PSD at $r = 8r_g$ (Figure 13, normalized such that a direct comparison can be made with the three-dimensional hydrodynamic results of Figure 8). It is important to note, however, that a trapped g -mode of the strength seen in our three-dimensional hydrodynamic simulation would not stand out from the background turbulence. Thus, while it is apparent that the fundamental trapped g -mode is not strongly excited by the turbulence (e.g., in the way that the local p -modes are), we cannot say whether the g -mode is actively damped by the turbulence.

Finally, we note that there is no indication that the parametric resonance instability of Abramowicz & Kluzniak is at work, at least in its simplest form. As discussed in Section 2, this model predicts its strongest resonance at the location where the radial and vertical epicyclic frequencies are in a 2:3 ratio; this occurs at $r = 9.2r_g$ in the PW potential. As shown in Figure 13, the PSD of the pressure fluctuations at $r = 9.2r_g$ shows no structure associated with the local epicyclic frequencies. We have verified that a similar conclusion holds true for the PSD of the other variables. While it is possible that nonlinear effects have shifted the location of the resonance inward from $r = 9.2r_g$ (A2003), we note that the PSDs of Figure 12 show no obvious

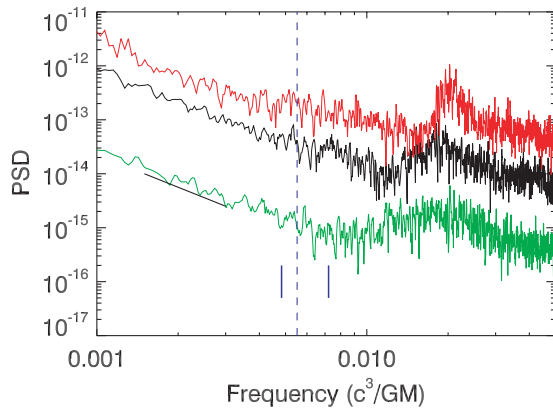


Figure 13. PSD of the midplane (decay-corrected) pressure for $\Delta r = 0.5r_g$ wide zones centered on $r = 7r_g$ (top red curve), $r = 8r_g$ (middle black curve), and $r = 9.2r_g$ (bottom green curve). The thin vertical dashed line marks the maximum radial epicyclic frequency. A line segment with a slope of -2 is shown for reference. Also shown (heavy vertical blue lines) are the radial and vertical epicyclic frequencies at $r = 9.2r_g$ where the simplest form of the parametric instability model would predict resonances.

(A color version of this figure is available in the online journal.)

radius at which the power at the radial epicyclic and the orbital frequencies appears to be locally enhanced.

4.4. Temporal Properties of the Instantaneous Black Hole Accretion Rate

The previous section addressed the temporal properties of the fundamental fluid variables through the body of the disk. Of course, real observations of accretion disks measure the electromagnetic radiation generated by the accretion flow. While our simulations miss all of the physics relevant for making a first-principles prediction of the observed light curve, it is still instructive to analyze a simple scalar quantity that can be generated from the simulation and may be related to the observed hard X-ray radiation (since it is the hard X-rays that carry the HFQPO signal).

Here we consider one such proxy for the observed light curve, the *instantaneous mass accretion rate* into the black hole,

$$\dot{M} = \int_{\partial\mathcal{R}_i} r(-v_r)\rho dS, \quad (22)$$

where the integral is performed over the surface $\partial\mathcal{R}_i$ defining the inner radial boundary of the computational domain. Figure 14 shows the raw light curve (i.e., not corrected for the exponential decay of the disk). In the remainder of this section, we address the temporal properties of this light curve. Of particular interest is the presence of breaks or QPOs in the PSD of this light curve. Hence, we need a quantitative approach by which the significance of such features in the PSD can be assessed. We begin by discussing our general statistical approach, which differs from that advocated by SKH.

4.4.1. Analysis Method

Our approach to PSD fitting is predicated on the assumption (also made by SKH) that at a given frequency, the power density has an exponential probability distribution; if the mean is p_0 , then the probability of measuring a power between p and $p + dp$ is

$$P(p)dp = \frac{1}{p_0} e^{-p/p_0} dp. \quad (23)$$

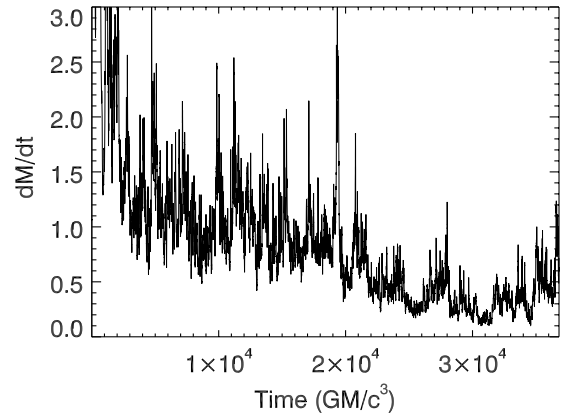


Figure 14. The instantaneous mass accretion rate onto the black hole from our canonical MHD simulation (run MHD_1).

Suppose that we have a model that predicts a power density $p_{\text{mod},i}$ for frequency bin i , and that in our MHD simulation, we actually observe a power density $p_{\text{obs},i}$ in that bin. Then the likelihood of the data given the model in that bin is

$$\mathcal{L}_i = (1/p_{\text{mod},i}) \exp(-p_{\text{obs},i}/p_{\text{mod},i}). \quad (24)$$

The likelihood of the whole power density spectrum given the model is the product of the individual likelihoods, but the log likelihood is typically more useful:

$$\ln \mathcal{L} = \sum_i [-\ln p_{\text{mod},i} - p_{\text{obs},i}/p_{\text{mod},i}]. \quad (25)$$

This is the figure of merit for a given model. It can, therefore, be used for standard tasks, such as parameter estimation and model comparison (e.g., determining if a QPO or break is required by the data).

Note that to maximize the information content, the bin size should be the smallest possible, in this case the frequency resolution of the raw PSD. As a result, this method does not require rebinning to coarser resolution. Our approach, therefore, yields an accurate evaluation of one or more precisely specified models, as opposed to the broader but less sensitive method of trying to detect a signal in a model-independent way.

We apply a Markov Chain Monte Carlo method to search for best fits and establish confidence regions. As discussed in Section 4.3.1, we correct for secular changes. Given the large amplitude fluctuations in the \dot{M} and S_{tot} curves, the endpoint method discussed in Section 4.3.1 is not appropriate. Hence, we employ the least-square method described in Section 4.3.1 in order to determine and then divide out the best-fitting exponential decay.

4.4.2. Results

The mass accretion rate \dot{M} has sufficient intrinsic variability that secular changes in the disk properties have only minor effects on the PSD. This is evident from Figure 15, which compares the PSD and Fourier phase of the raw \dot{M} curve as a function of frequency (left panel) with these after multiplication by the exponential in time that minimizes the overall rms amplitude (right panel). The lack of significant differences suggests that inferences drawn from the PSD are robust. The comparison shown in Figure 15 is for the second quarter of run MHD_1 (approximately $t = 150T_{\text{isco}}$ to $t = 310T_{\text{isco}}$); analyses of the third and fourth quarters also reveal a lack of sensitivity to the secular decay of the disk.

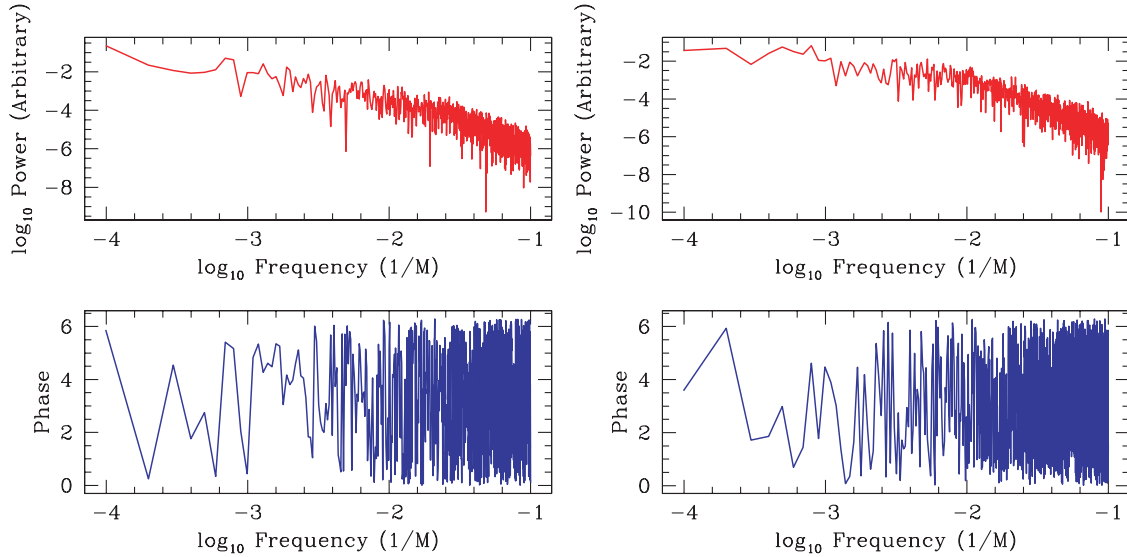


Figure 15. Comparison of the PSD and Fourier phase of the mass accretion rate without (left panel) and with (right panel) multiplication of the time series by an exponential in time designed to compensate for the slow loss of mass from the disk. The similarity of the two implies that at these frequencies, the variability is dominated by intrinsic fluctuations instead of by secular changes in the disk.

(A color version of this figure is available in the online journal.)

Table 2
Model Comparisons for PSD of Mass Accretion Rate \dot{M}

Data segment	Model	Parameters and Uncertainties	Maximum $\ln \mathcal{L}$
1	Single PL	$\Gamma = 2.50 \pm 0.05$	9131
	Broken PL	$\Gamma_1 = 0.82 \pm 0.09, \Gamma_2 = 2.96 \pm 0.07,$ $\log_{10}(\nu_{\text{break}}) = -1.94 \pm 0.04$	9238
2	Single PL	$\Gamma = 2.70 \pm 0.08$	6508
	Broken PL	$\Gamma_1 = 1.45 \pm 0.11, \Gamma_2 = 2.91 \pm 0.10,$ $\log_{10}(\nu_{\text{break}}) = -1.65 \pm 0.07$	6609
3	Single PL	$\Gamma = 2.16 \pm 0.04$	9561
	Broken PL	$\Gamma_1 = 1.47 \pm 0.07, \Gamma_2 = 2.89 \pm 0.09,$ $\log_{10}(\nu_{\text{break}}) = -1.60 \pm 0.04$	9630

Note. Γ is the power-law index of a single power-law model for the PSD; $P(\nu) \propto \nu^{-\Gamma}$. Γ_1 and Γ_2 are the two indices obtained from a broken power law; $P \propto \nu^{-\Gamma_1}$ for $\nu < \nu_{\text{break}}$ and $P \propto \nu^{-\Gamma_2}$ for $\nu > \nu_{\text{break}}$. All error bars are 1 standard deviation.

Having established that the secular decay of the disk is unimportant for the PSD of \dot{M} , we will directly work with the raw time series from run MHD_1, without multiplication by an exponential function. We separately analyze the second, third, and fourth quarters of the data (each encompassing a period of $\Delta t \approx 160T_{\text{ISCO}}$) to look for trends or stability in the PSD, while discarding the first quarter as potentially biased by initial conditions. The results are summarized in Table 2, where we compare single power-law models for the PSD with models involving a broken power law. We use the method described in the previous section; note that only differences in the log likelihood $\ln \mathcal{L}$ are important rather than the absolute magnitude of $\ln \mathcal{L}$.

From this analysis, we find compelling evidence of a break in the power law characterizing the PSD of \dot{M} . Compared with a single power law, the broken power fit is better by $\Delta \ln \mathcal{L} = 76-90$; hence, the maximum likelihood ratio is at least $\exp(76) = 10^{33}$ in all three data segments independently. The break frequency and power-law slopes are consistent between the second and third data segments, but these do not match the first data segment. The break frequencies are within a factor of 2 of, but not consistent with, the orbital frequency at the ISCO, $\log_{10}(\nu_{\text{ISCO}}) = -1.79$. Therefore, although there is a clear

steepening in the power density spectrum, it is not possible at this point to assign a specific physical meaning to the break. We note that this general form of the PSD, that is, an approximate power law with curvature or a break at frequencies close to the ISCO orbital frequency, has been previously seen in the mass accretion rate of global disk simulations (Hawley & Krolik 2001, 2002).

We see no indications of QPOs in the \dot{M} PSD. Quantitatively, we add a Lorentzian QPO to the broken power-law PSD model in which the QPO centroid frequency, FWHM, and amplitude are allowed to be free parameters, with the one restriction that the quality factor of the QPO must exceed 2. We find that the peak power of any QPO cannot exceed 2% of the continuum power measured at the centroid of the QPO at the 99% confidence level.

5. DISCUSSION

5.1. Comparison with Previous Numerical Results

In recent years, several groups have reported temporal analyses of MHD disk simulations. Here, we briefly compare our work with some of these published results.

Probably the most relevant previous work is that of Arras et al. (2006; hereafter ABT). These authors perform a local, shearing box MHD simulation of a patch of an accretion disk;

this provides a controlled environment in which fluid modes can be characterized. ABT found that the MHD turbulence excites a spectrum of distinct acoustic modes as well as radial epicyclic motions. However, they noted a lack of distinct inertial modes (g -modes) and used this fact to argue against the excitation of trapped g -modes in global accretion disks. Our findings are completely in line with those of ABT, and represent an extension of ABT's conclusions to global simulations of thin accretion disks.

There have been QPOs reported from global simulations. Kato (2004d) performed a global MHD disk simulation in a PW potential and presented an analysis of quantities derived from the mass accretion rate. Through visual inspection of the resulting PSDs from four periods of the (long) simulation, he reported a pair of transient QPOs and a pair of QPOs that are labeled as persistent (although it is not clear that they are present in the PSD of all data segments, and the statistical significance of the features is unclear). The QPOs are attributed to resonances between the vertical and radial epicyclic frequencies, and it is found that these QPO pairs have frequency ratios that are *approximately* 3:2. We find no evidence of these resonances in our simulations. In another interesting difference, an inspection of the radially resolved PSDs in Kato (2004d) reveal no signs of the local p -modes that seem to feature so prominently in our PSDs. While the reason for these discrepancies is unclear, we do note that the Kato (2004d) simulations have an order-of-magnitude less resolution in both the azimuthal and (more importantly) the vertical directions, although his simulations do have a significantly larger computational domain. It is possible that the Kato (2004d) simulations have failed to adequately resolve the vertical dynamics of the thin disk.

Chan et al. (2006) have also performed global MHD disk simulations in a PW potential using the pseudo-spectral algorithm of Chan et al. (2005, 2006). Their study included a postprocessing of the simulation to include detailed radiative transfer, and was explicitly targeted at understanding the variability (including the large amplitude flaring) of the hot accretion flow around the black hole at the center of the Galaxy. They found that the turbulence of the quiescent flow could only produce a factor of 2 modulations in the observed luminosity. To model the large amplitude flares, they introduced large density perturbations into the flow. After being perturbed, the disk displays a QPO with a frequency equal to the orbital frequency at the magnetosonic point. Given that the Chan et al. study explores a rather different regime of accretion than our present study (i.e., hot, thick accretion flows versus thin, cold accretion flows), it is hard to make a direct comparison.

Finally, SKH have performed detailed analyses of General Relativistic MHD (GRMHD) simulations of disks performed using the code of De Villiers & Hawley (2003). In particular, they have studied a long ($6000 GM/c^3$) simulation of a disk around a Schwarzschild black hole, focusing on the temporal behavior of proxy light curves (rather than the underlying fluid properties discussed in this paper). It is unclear from their analysis whether their simulated accretion disk has excited local p -modes of the type that we find in this current work. SKH did find, though, that a proxy light curve based on radiative transfer through the disk assuming black body emission and free-free absorption displays QPOs with an approximate 3:2 ratio. However, these QPOs are transient, only appearing at certain times and certain viewing inclinations.

5.2. Comments on 3:2 Frequency Ratios

As described above, several authors have reported transient QPO pairs from MHD simulations with a frequency ratio of 3:2.

It is tempting to interpret these as resonance phenomena. Here, we note that there are several ways that approximate 3:2 ratios can be generated that do not necessarily involve resonances and, hence, one should guard against overinterpreting QPO pairs. Indeed, we must remember that some sources have QPO frequency ratios that are inconsistent with 3:2 (e.g., the 67 Hz and 41 Hz QPOs from GRS 1915+105; see Strohmayer 2001).

For example, consider the local vertical p -modes of the disk (discussed in Section 2.1). At a given radius, the $n = 1$ vertical pressure mode has a frequency of $\omega_{\text{vert},1} = \sqrt{\gamma + 1} \Omega$, where Ω is the orbital frequency. For a gas-pressure-dominated disk in which $\gamma = 5/3$, $\omega_{\text{vert},1}/\Omega = 1.63$, and for a radiation pressure dominated disk in which $\gamma = 4/3$, $\omega_{\text{vert},1}/\Omega = 1.53$. If some unspecified physical process enhances emission from a given ring of the disk, one can imagine a situation where QPOs are generated at the orbital frequency and the $n = 1$ vertical pressure mode, thereby giving frequency ratios compatible with the measured ratios in several sources. Alternatively, the next lowest vertical mode that has a vertical velocity node in the midplane (and thus the maximum variation of pressure and density there) has a frequency of $\omega_{\text{vert},3} = \sqrt{3\gamma + 1} \Omega$. As a result, when $\gamma = 5/3$, we have $\omega_{\text{vert},3}/\omega_{\text{vert},1} = 1.5$, and when $\gamma = 4/3$, the ratio is 1.46. Once again, if nature picks out a specific radius and the emission is modulated by the $n = 1$ and $n = 3$ modes, we would see QPOs with frequency ratios entirely consistent with the observations.

As another example, suppose that the disk emission is modulated at the vertical and radial epicyclic frequencies and that the emission is distributed in radius according to a standard Page & Thorne (1974) disk. The radial distribution of the emission then peaks close to the radius where the radial epicyclic frequency is a maximum (and, hence, is slowly changing with radius). One might then expect to see a pair of QPOs corresponding to these two epicyclic frequencies. The frequency ratio only weakly depends on the spin parameter, ranging from 1.46 at $a/M = 0$ to 1.7 at $a/M = 0.9$.

6. CONCLUSIONS

The origin of HFQPOs remains elusive. Our simulations of geometrically thin accretion disks have shown that MRI-driven MHD turbulence does not excite the trapped g -modes of NW92, even when these modes definitively exist in the equivalent hydrodynamic disk. We have also shown that MHD turbulence does not excite the parametric resonance instability of Abramowicz & Kluźniak (2001). Instead, the only distinct modes found in our simulated MHD disks are local vertical p -modes and radial epicyclic oscillations.

Clearly, the failure of all simulations to date to produce stable QPO pairs of the type seen in GBHBs suggests that either the QPOs are too weak to be detected in the simulations or the models are missing some important physical ingredients. It is an open question whether the global disk modes or the parametric instabilities discussed in this paper can be excited once one includes the full effects of GR close to rapidly spinning black holes and/or radiation physics. Indeed, the fact that HFQPOs are only seen in rather special spectral states (the soft intermediate state; e.g., see Belloni 2006), when the accretion rate is thought to be comparable with the Eddington limit, suggests that radiation physics, in particular, may well be important to the HFQPO mechanism. It is also noteworthy that the transition from the hard intermediate state into the soft intermediate state is associated with powerful relativistic ejection events. Thus, another interesting possibility is that

HFQPO production occurs in the black hole magnetosphere (i.e., the base of the jet) and not the accretion disk at all.

We thank E. Ostriker for insightful discussions as well as allowing us the use of her MPI-parallelized version of ZEUS. We are also grateful to A. Fabian, G. Ogilvie, S. O'Neill, J. Pringle, J. Miller, P. Uttley, S. Vaughan, and B. Wagoner for comments and discussion that significantly improved this paper. All simulations described in this paper were performed on the Beowulf cluster ("The Borg") supported by the Center for Theory and Computation (CTC) in the Department of Astronomy at the University of Maryland College Park. C.S.R. and M.C.M. thank the National Science Foundation for support under grant AST 06-07428. C.S.R. also gratefully acknowledges the University of Maryland's Graduate Research Board Semester Award Program, which supported the early phases of this work.

APPENDIX A

FUNDAMENTAL g -MODE FREQUENCY FOR VERY SMALL SOUND SPEEDS

For very small sound speeds, there are simplifications that allow the frequency of the fundamental trapped g -mode in a hydrodynamic accretion disk to be analytically obtained. Here, we base our analysis on the equations and formalism of NW92.

NW92 examined the linearized equations describing the behavior of the scalar potential

$$\delta u \equiv \delta P / \rho, \quad (\text{A1})$$

where δP is the Eulerian variation in the pressure. The radial equation for the perturbation is

$$\omega^2 c_s^2 \frac{\partial^2 \delta u}{\partial r^2} = -(\omega^2 - \gamma \Upsilon \Omega^2) (\omega^2 - \kappa^2) \delta u, \quad (\text{A2})$$

where ω is the mode angular frequency, Ω is the orbital angular frequency, κ is the radial epicyclic angular frequency, and γ is the usual adiabatic index $\gamma = 5/3$. Υ is determined by the quantization condition

$$\frac{A + 1/2}{(1 - 4B)^{1/2}} = j + 1/2, \quad (\text{A3})$$

where $A = \Upsilon - \zeta$ and

$$B = \frac{\zeta (\omega^2 - \gamma \Upsilon \Omega^2)}{\omega^2} \quad (\text{A4})$$

with $\zeta = (\gamma - 1)/\gamma = 2/5$. For the fundamental mode, we have $j = 0$ and Equation (A3) can be solved to obtain

$$\Upsilon = 0.4 \frac{\Omega^2}{\omega^2} - 0.2. \quad (\text{A5})$$

Now we concentrate on low sound speeds, $c_s \ll 1$ (within this appendix, speeds will be given in units of c , frequencies in units of $c^3/(GM)$, and lengths in units of r_g). This implies that the mode frequency $\omega \approx \kappa_{\max}$, where κ_{\max} is the maximum radial epicyclic frequency. In this limit, we note that the factor $(\omega^2 - \gamma \Upsilon \Omega^2)$ within Equation (A2) is close to constant with radius. Let us define $D \equiv -(\omega^2 - \gamma \Upsilon \Omega^2) > 0$, where we evaluate D by assuming $\omega = \kappa_{\max}$.

We also note that near the maximum, the radial epicyclic frequency has a parabolic form, $\kappa^2 = \kappa_{\max}^2 - E(r - r_{\max})^2$,

where r_{\max} is the radius at which $\kappa = \kappa_{\max}$. The differential equation then becomes

$$\frac{\partial^2 \delta u}{\partial r^2} = \left[-\frac{D}{c_s^2} (\kappa_{\max}^2 / \omega^2 - 1) + \frac{D}{c_s^2} \frac{E}{\omega^2} (r - r_{\max})^2 \right] \delta u. \quad (\text{A6})$$

This has the form of a harmonic oscillator, so we try a solution of the type

$$\delta u \propto e^{-\frac{1}{2} C (r - r_{\max})^2}, \quad (\text{A7})$$

meaning that

$$\frac{\partial^2 \delta u}{\partial r^2} = [C^2 (r - r_{\max})^2 - C] e^{-\frac{1}{2} C (r - r_{\max})^2}. \quad (\text{A8})$$

This yields the conditions

$$C = \frac{D}{c_s^2} (\kappa_{\max}^2 / \omega^2 - 1) \quad (\text{A9})$$

$$C^2 = \frac{D}{c_s^2} \frac{E}{\omega^2}. \quad (\text{A10})$$

$$(\text{A11})$$

Defining $x \equiv 1/\omega^2$, these two conditions can be combined (eliminating C) to yield

$$\frac{D^2}{c_s^4} (\kappa_{\max}^4 x^2 - 2\kappa_{\max}^2 x + 1) = \frac{D}{c_s^2} E x. \quad (\text{A12})$$

Solving for x gives

$$x = \frac{1}{2\kappa_{\max}^4} \left[2\kappa_{\max}^2 + c_s^2 E / D \pm \sqrt{4\kappa_{\max}^2 c_s^2 E / D + c_s^4 E^2 / D^2} \right]. \quad (\text{A13})$$

Since $\omega < \kappa_{\max}$, we choose the positive sign. For small c_s , the first term in the square root dominates, and the lowest order in c_s gives

$$x \approx \frac{1}{\kappa_{\max}^2} \left(1 + \frac{c_s}{\kappa_{\max}} \sqrt{\frac{E}{D}} \right). \quad (\text{A14})$$

This finally implies that

$$\frac{\kappa_{\max} - \omega}{\kappa_{\max}} = \frac{c_s}{2\kappa_{\max}} \sqrt{E/D}. \quad (\text{A15})$$

This clearly demonstrates that the fractional difference of the mode frequency from the radial epicyclic maximum is linear in c_s .

Evaluating this expression for the PW potential, we obtain $\kappa_{\max}^2 = 1.202 \times 10^{-3}$ (at $r = r_{\max} = 4 + 2\sqrt{3} = 7.464$), and

$$\frac{\kappa_{\max} - \omega}{\kappa_{\max}} = 2.269 c_s. \quad (\text{A16})$$

In contrast, the Nowak & Wagoner pseudo-Newtonian potential,

$$\Phi_{\text{NW}} = -\frac{1}{r} + \frac{3}{r^2} - \frac{12}{r^3}. \quad (\text{A17})$$

yields $\kappa_{\max}^2 = 8.607 \times 10^{-4}$ (at $r_{\max} = 7.746$) and

$$\frac{\kappa_{\max} - \omega}{\kappa_{\max}} = 5.621 c_s. \quad (\text{A18})$$

For both potentials, the analytical frequencies agree extremely well with direct numerical solutions to Equation (A2).

REFERENCES

- Abramowicz, M. A., Almergren, G. J. E., Kluźniak, W., Thampan, A. V., & Wallinder, F. 2002, *Class. Quantum Grav.*, **19**, L57
- Abramowicz, M. A., Karas, V., Kluźniak, W., Lee, W. H., & Rebusco, P. 2003, *PASJ*, **55**, 467 (A2003)
- Abramowicz, M. A., & Kluźniak, W. 2001, *A&A*, **374**, L19
- Abramowicz, M. A., & Kluźniak, W. 2003, *Gen. Rel. Grav.*, **35**, 69
- Arras, P., Blaes, O. M., & Turner, N. J. 2006, *ApJ*, **645**, L65 (ABT)
- Balbus, S. A., & Hawley, J. F. 1991, *ApJ*, **376**, 214
- Balbus, S. A., & Hawley, J. F. 1998, *Rev. Mod. Phys.*, **70**, 1
- Belloni, T. 2006, *Adv. Space Res.*, **38**, 2801
- Binney, J., & Tremaine, S. 1987, *Galactic Dynamics* (Princeton, NJ: Princeton Univ. Press), 359
- Chan, C. K., Psaltis, D., & Özel, F. 2005, *ApJ*, **628**, 353
- Chan, C. K., Psaltis, D., & Özel, F. 2006, *ApJ*, **645**, 506
- Chan, C. K., et al. 2006, *ApJ*, submitted (arXiv:0611269)
- Cowling, T. G. 1957, *Q. J. Mech. Appl. Math.*, **10**, 129
- De Villiers, J.-P., & Hawley, J. F. 2003, *ApJ*, **592**, 1060
- Friedman, J. L., & Schutz, B. F. 1978, *ApJ*, **221**, 937
- Gammie, C. F., McKinney, J. C., & Tóth, G. 2003, *ApJ*, **589**, 444
- Gierlinski, M., Middleton, M., Ward, M., & Done, C. 2008, *Nature*, **455**, 369
- Hantao, J., Burin, M., Schartman, E., & Goodman, J. 2006, *Nature*, **444**, 343
- Hawley, J. F., Gammie, C. F., & Balbus, S. A. 1996, *ApJ*, **464**, 690
- Hawley, J. F., & Krolik, J. H. 2001, *ApJ*, **548**, 348
- Hawley, J. F., & Krolik, J. H. 2002, *ApJ*, **566**, 164
- Kato, S. 1990, *PASJ*, **42**, 99
- Kato, S. 1991, *PASJ*, **43**, 557
- Kato, S. 1993, *PASJ*, **45**, 219
- Kato, S. 2004a, *PASJ*, **56**, 559
- Kato, S. 2004b, *PASJ*, **56**, 905
- Kato, S. 2004c, *PASJ*, **56**, L25
- Kato, S., & Fukue, J. 1980, *PASJ*, **322**, 377
- Kato, S., & Honma, F. 1991, *PASJ*, **43**, 95
- Kato, Y. 2004d, *PASJ*, **56**, 931
- Lehr, D., Wagoner, R. V., & Wilms, J. 2000, arXiv:astro-ph/0004211
- Lubow, S. H., & Pringle, J. E. 1993, *ApJ*, **409**, 360 (LP93)
- Marković, D., & Lamb, F. K. 1998, *ApJ*, **507**, 316
- McClintock, J., & Remillard, R. 2006, in *Compact Stellar X-ray Sources*, ed. W. H. G. Lewin, & M. van der Klis (Cambridge: Cambridge Univ. Press), 157
- McClintock, J. E., & Remillard, R. A. 2003, arXiv:astro-ph/0306213
- McHardy, I. M., Körding, E., Knigge, C., Uttley, P., & Fender, R. P. 2006, *Nature*, **444**, 730
- Miller, K. A., & Stone, J. M. 2000, *ApJ*, **534**, 398
- Nowak, M. A., & Wagoner, R. V. 1991, *ApJ*, **378**, 656 (NW91)
- Nowak, M. A., & Wagoner, R. V. 1992, *ApJ*, **393**, 697 (NW92)
- Nowak, M. A., & Wagoner, R. V. 1993, *ApJ*, **418**, 187
- Nowak, M. A., Wagoner, R. V., Begelman, M. C., & Lehr, D. E. 1997, *ApJ*, **477**, L91
- Okazaki, A. T., Kato, S., & Fukue, J. 1987, *PASJ*, **39**, 457
- Ortega-Rodríguez, M., Silbergleit, A. S., & Wagoner, R. V. 2001, *ApJ*, **567**, 1043
- Paczynski, B., & Wiita, P. J. 1980, *A&A*, **88**, 23 (PW)
- Page, D. N., & Thorne, K. S. 1974, *ApJ*, **191**, 499
- Perez, C. A., Silbergleit, A. S., Wagoner, R. V., & Lehr, D. E. 1997, *ApJ*, **476**, 589
- Reynolds, C. S., & Fabian, A. C. 2008, *ApJ*, **675**, 1048
- Rezzolla, L., Yoshida, S., Maccarone, T. J., & Zanotti, O. 2003a, *MNRAS*, **344**, L37
- Rezzolla, L., Yoshida, S., & Zanotti, O. 2003b, *MNRAS*, **344**, 978
- Schnittman, J. D., Krolik, J. H., & Hawley, J. F. 2006, *ApJ*, **651**, 1031 (SKH)
- Shafee, R., McKinney, J. C., Narayan, R., Tchekhovkoy, A., Gammie, C. F., & McClintock, J. E. 2008, *ApJ*, **687**, L25
- Shakura, N. I., & Sunyaev, R. A. 1973, *A&A*, **24**, 337
- Silbergleit, A. S., Wagoner, R. V., & Ortega-Rodríguez, M. 2001, *ApJ*, **548**, 335
- Stone, J. M., Hawley, J. F., Gammie, C. F., & Balbus, S. A. 1996, *ApJ*, **463**, 656
- Stone, J. M., & Norman, M. L. 1992a, *ApJS*, **80**, 753
- Stone, J. M., & Norman, M. L. 1992b, *ApJS*, **80**, 791
- Strohmayer, T. E. 2001, *ApJ*, **554**, L169
- Uttley, P., & McHardy, I. M. 2001, *MNRAS*, **323**, L26
- Uttley, P., McHardy, I. M., & Vaughan, S. 2005, *MNRAS*, **359**, 345
- Vernaleo, J. C., & Reynolds, C. S. 2006, *ApJ*, **645**, 83
- Wagoner, R. V., Silbergleit, A. S., & Ortega-Rodríguez, M. 2001, *ApJ*, **559**, L25